



IMEX_SfloW2D v2: a depth-averaged numerical flow model for volcanic gas-particle flows over complex topographies and water

Mattia de' Michieli Vitturi¹, Tomaso Esposti Ongaro¹, and Samantha Engwell²

¹Istituto Nazionale di Geofisica e Vulcanologia, Sezione di Pisa, Pisa, Italy

²British Geological Survey, The Lyell Centre, Research Avenue South, Edinburgh, UK

Correspondence: Mattia de' Michieli Vitturi (mattia.demichielivitturi@ingv.it)

Abstract. We present developments to the physical model and the open source numerical code IMEX_SfloW2D (de' Michieli Vitturi et al., *Geosci. Mod. Devel.*, 2019). These developments consist of a generalization of the depth-averaged (shallow-water) fluid equations to describe a polydisperse fluid-solid mixture, including terms for sedimentation and entrainment, transport equations for solid particles of different sizes, transport equations for different components of the carrier phase, and an equation for temperature/energy. Of relevance for the simulation of volcanic mass flow, vaporization and entrainment of water are implemented in the new model. The model can be easily adapted to simulate a wide range of volcanic mass flows (pyroclastic avalanches, lahars, pyroclastic surges) and here we present its application to transient dilute pyroclastic density currents (PDCs). The numerical algorithm and the code have been improved to allow for simulation of sub- to supercritical regimes and to simplify the setting of initial and boundary conditions. The code is open-source. The results of synthetic numerical benchmarks demonstrate the robustness of the numerical code in simulating trans-critical flows interacting with the topography. Moreover, they highlight the importance of simulating transient in comparison to steady-state flows, and flows in 2D versus 1D. Finally, simulation of the Krakatau 1883 eruption demonstrates the capability of the numerical model to face a complex natural case involving the propagation of PDCs over the sea surface and across topographic obstacles, showing the relevance, at the large scale, of non-linear fluid dynamic features, such as hydraulic jumps and Van Karman vortexes to flow conditions such as velocity and runout.

1 Introduction

In the past decades, the development of numerical models for geophysical mass flows and their application to hazard assessment has seen a rapid growth. Better understanding of the physics governing such flows has enabled development of more accurate models while a tremendous increase in computational resources has made increasingly high-resolution numerical simulations possible. Despite these advances, for some applications, there is still the need for simplified and fast models. This is true, for example, for forecasting and hazard quantification purposes, where a probabilistic approach generally requires a large number (thousands or more) of simulations in a relatively short time frame.

For a large class of geophysical mass flows, characterized by having the horizontal length scale much greater than vertical one, it is possible to reduce the dimensionality of the problem (and thus the computational cost of its numerical solution)



25 by adopting the so-called Shallow Water Equations approach. The shallow-water equations are a set of partial differential equations that describe fluid flow problems, originally introduced by Adhemar Jean Claude Barre de Saint-Venant, obtained by the averaging of a flows variables over its thickness, thus reducing the model complexity (Pudasaini and Hutter, 2007; Toro, 2013). Shallow-water equations have been applied successfully to tsunamis (Fernández-Nieto et al., 2008), atmospheric flows (Zeitlin, 2018), storm surges (Von Storch and Woth, 2008), landslides and debris flows (Iverson and Denlinger, 2001; Denlinger and Iverson, 2001), snow and rock avalanches (Bartelt et al., 1999; Christen et al., 2010) and planetary flows (Iga and Matsuda, 2005). In the volcanological field, shallow-water equations have been applied to the umbrella cloud spreading (Johnson et al., 2015; de' Michieli Vitturi and Pardini, 2021), lahars (Fagents and Baloga, 2006; O'Brien et al., 1993), pyroclastic density currents (Pitman et al., 2003; Patra et al., 2005; Capra et al., 2008; Calabrò et al., 2022; Kelfoun et al., 2009; de' Michieli Vitturi et al., 2019; Shimizu et al., 2017a) and lava flows (Costa and Macedonio, 2005; Biagioli et al., 2021; Hyman et al., 2022).

35 Another common feature of most geophysical flows is that they are multiphase flows, with a continuous carrier phase (gas or liquid) and a solid dispersed phase. For the numerical modeling of such multiphase flows two main approaches can be adopted, with the solid phase treated as a continuum (Eulerian approach) or as discrete elements for which the equations of motion are solved (Lagrangian approach). The latter approach is better suited for low particle concentration and when the particle relaxation time, quantified by the inertial effect of particles, is much smaller than the characteristic time of collisions between particles (Dufek, 2015; Neri et al., 2022). For the volcanological applications of interest here (dilute pyroclastic density currents, or PDC), the flow can be highly turbulent favouring particle collisions, and thus the continuum approach is appropriate. Most of these flows can be described and modeled using the full 3D transient multiphase Navier-Stokes equations but, since the numerical three-dimensional calculation is still very costly, it makes sense to reduce the equations for calculations with simpler flow conditions.

45 In this work, we present a new version of IMEX-SfloW_2D (de' Michieli Vitturi et al., 2019), a depth-averaged model originally developed for the simulation of pyroclastic avalanches, i.e. a type of granular flow characterized by relatively thin layers at high particle concentration (10–50 vol %). Similarly to other codes used in volcanological research and applications such as Volcflow (Kelfoun and Druitt, 2005), TITAN2D (Pitman et al., 2003; Patra et al., 2005), and SHALTOP (Bouchut and Westdickenberg, 2004; Mangeney et al., 2007), IMEX-SfloW_2D is a shallow-water equations model based on depth-averaging, obtained by integrating the full 3D equations along the vertical dimension. With respect to the original version of the model (de' Michieli Vitturi et al., 2019), where the granular mixture was described as a single-phase mono-disperse granular fluid ignoring the presence of the interstitial gas, here the formulation and the equations have been generalized to a fluid-solid mixture, also adding sedimentation and entrainment terms, transport equations for the solid particles of different sizes, transport equations for different components of the carrier phase, and an equation for temperature/energy.

55 The model framework is general and, by changing the constitutive equations defining phase properties and flow rheology, it is possible to simulate a variety of geophysical flows. However, in this paper we focus our attention on the modeling of PDCs, i.e. flows of gas and pyroclasts (fragments of volcanic rocks produced by explosive fragmentation), and in particular dilute PDCs, which are characterized by densities of less than 10 kg/m^3 (roughly corresponding to a particle volume fraction of less



than approximately 0.01). This hypothesis allows us to neglect the influence of particle-particle friction and the internal stress
60 tensor.

Dilute PDCs can form in relation to several volcanic behaviours (Valentine, 1987; Branney and Kokelaar, 2002; Sulpizio
et al., 2014; Dufek et al., 2015), including the collapse of Plinian and Vulcanian columns, and the explosive fragmentation of a
lava dome or cryptodome (Sigurdsson et al., 2015). Irrespective of the generating mechanism, dilute PDC propagation regimes
65 can be characterized by the flow Richardson number (Ri), expressing the ratio between the potential energy and the kinetic
energy available for mixing or, in other terms, the ratio between the relative celerity of surface waves and the velocity of the flow
(Chow, 1959). Dilute PDCs may propagate as either subcritical ($Ri > 1$) or supercritical ($Ri < 1$) flows (Bursik and Woods,
1996), and they can also experience transitions from one regime to the other. For supercritical flows, where the speed of the
flow is greater than the speed of gravity waves, entrainment is significant and the runout distance tends to be shorter. As large
amounts of ambient air are entrained into the flow, ash particles elutriate to form a coignimbrite column (Bursik and Woods,
70 1996; Engwell et al., 2016). Conversely, subcritical flows, where the velocity of the flow is low enough for internal waves to
propagate in either direction, have negligible entrainment and tend to have longer runout distances. The capability of dilute
flows to overcome topographic barriers, and consequently the sedimentation regimes, also depends on the Richardson number
(Woods and Wohletz, 1991; Woods et al., 1998). For these reasons, an accurate description of these regimes is mandatory for
a model of dilute PDCs, both in the definition of the equations and in their numerical discretization and solution.

75 In this work, Sections 2 and 3 are devoted to the presentation of the new physical model for dilute PDCs based on the
shallow-water approximation. The new model extends previous similar models by describing a polydisperse fluid-solid mixture
with sedimentation and entrainment terms, transport equations for the solid particles of different sizes, transport equations for
different components of the carrier phase, and an equation for temperature/energy. Moreover, it accounts for the potential
vaporization of liquid water and entrainment of water vapour into the current. Section 4 summarizes the main aspects of the
80 numerical algorithm, with emphasis on those details that are relevant for resolving the sub- supercritical transitional regimes.
We devote Section 5 to the application of the model to one-dimensional literature benchmark tests (Delestre et al., 2013),
in order to show the capability of the code to properly simulate the different flow regimes. For supercritical conditions, we
also present two 2D test cases, derived from Engwell et al. (2016). These tests show that the steady conditions reached by
the simulation after the initial transient phase correspond to those obtained with the 1D steady model presented in Engwell
85 et al. (2016) and based on Bursik and Woods (1996). Finally, in Section 6 the model is applied to the 1883 Krakatau eruption.
This is an original study on the propagation of PDCs over water, with a complex 3D topography and display of complex
super/subcritical regime transitions, well representing the complexity of PDC dynamics in real cases. For this example, a 30m
SRTM DEM of the area is used, which allows us to simulate the effects of real topographic obstacles on the flow propagation
and understand how they control the flow regime.

90 Most of the examples presented in this work, as well as the source code, can be freely downloaded from the model repository
at github.com/demichie/IMEX_SfloW2D_v2. The Github repository also contains pre- and post-processing Python scripts,
both general and specific for the included examples. The repository and the codes (Fortran main code and Python utility
scripts) are compliant with the set of standards defined by the European Open Science Cloud (EOSC) Synergy (SQAaas gold



badge) which assigned, through a Quality Assessment & Awarding (QAA), a SQAAs Gold Badge. The compiled code is also
 95 available as a Docker container at the following link: hub.docker.com/r/demichie/imex_sflow2d_v2.

2 The physical model

We describe here the equations adopted to describe a gas-particle flow with temperature-dependent mixture density, under the
 assumption that the flow propagates at atmospheric pressure, and that the effects of compressibility are negligible. In addition,
 we adopt a physical formulation based on depth averaging of the flow variables, which is appropriate for shallow flows and is
 100 computationally less expensive than considering density and velocity variation with depth.

The model is based on the Saint-Venant equations (Pudasaini and Hutter, 2007; Toro, 2013), coupled with source terms
 describing the entrainment/loss of mass and frictional forces, and enriched with an energy equation and with transport equations
 for different flow phases/components. In fact, we assume that the flow is a homogeneous mixture of a multi-component gas
 phase (air and water vapour) and n_s dispersed solid phases. The density of the mixture $\rho_m(x, y, t)$ is defined in terms of the
 105 volumetric fractions $\alpha_{(\cdot)}$ and densities $\rho_{(\cdot)}$ of the components:

$$\rho_m = \alpha_a \rho_a + \alpha_{wv} \rho_{wv} + \sum_{i_s=1}^{n_s} \alpha_{s,i_s} \rho_{s,i_s}, \quad (1)$$

where the subscript a denotes the air component, the subscript wv denotes the water vapour component, and the subscript
 s_{i_s} denote the class $i_s = 1, \dots, n_s$ of the solid phases. Each solid class is characterized by its diameter d_{i_s} , density ρ_{s,i_s} , and
 specific heat C_{s,i_s} . For a full list of model variables and notation, please refer to Table 1.

110 Equations are written in global Cartesian coordinates, with x and y orthogonal to the z -axis, parallel to gravitational
 acceleration $\mathbf{g} = (0, 0, g)$. We denote the flow thickness (parallel to the vertical z -axis) with $h(x, y, t)$ and the horizontal
 components of the flow velocity with $u(x, y, t)$ and $v(x, y, t)$ (averaged over the vertical flow thickness). The flow moves over
 a topography $B(x, y, t)$, and we allow the topography to change with time (for example, by particle sedimentation).

Conservation of mass for the flow is calculated:

$$115 \frac{\partial \rho_m h}{\partial t} + \frac{\partial (\rho_m h u)}{\partial x} + \frac{\partial (\rho_m h v)}{\partial y} = - \sum_{i_s=1}^{n_s} [\rho_{s,i_s} D_{s,i_s}] + \rho_a E_a + \rho_{wv}^b E_{wv}, \quad (2)$$

where D_s is the volumetric rate of deposition of solid particles, E_a is the volumetric air entrainment rate from the atmosphere,
 and E_{wv} is the volumetric water vapour entrainment, which could occur for flows over water bodies (sea or lakes). These rates
 are defined per unit surface area, and thus have units ms^{-1} . We assume that the density ρ_{wv}^b of water vapour ingested into the
 flow is not that corresponding to flow temperature, but at boiling temperature.

120 Introducing the notation g' for the reduced gravity $g' = [(\rho_m - \rho_a)/\rho_m]g$, the equations for the momentum components are:

$$\frac{\partial (\rho_m h u)}{\partial t} + \frac{\partial}{\partial x} \left(\rho_m h u^2 + \rho_m g' \frac{h^2}{2} \right) + \frac{\partial}{\partial y} (\rho_m h u v) = -\rho_m g' h \frac{\partial B}{\partial x} + F_x - u \sum_{i_s=1}^{n_s} (\rho_{s,i_s} D_{s,i_s}), \quad (3)$$



$$\frac{\partial(\rho_m h v)}{\partial t} + \frac{\partial}{\partial x}(\rho_m h u v) + \frac{\partial}{\partial y} \left(\rho_m h v^2 + \rho_m g' \frac{h^2}{2} \right) = -\rho_m g' h \frac{\partial B}{\partial y} + F_y - v \sum_{i_s=1}^{n_s} (\rho_{s,i_s} D_{s,i_s}), \quad (4)$$

where F_x and F_y represent the friction terms. Eqs. 3 and 4 are derived in the so-called hydrostatic approximation, i.e., the variation of momentum in the z direction are neglected and pressure is always hydrostatic. There are no terms associated with air and water vapour entrainment, because they do not carry any horizontal momentum into the flow.

Density of the gas components is a function of the flow temperature T , which changes with entrainment of external air. In addition, part of the thermal energy of particles lost when the current travels over water produces steam which can be entrained in the flow. For this reason, with respect to the classical incompressible shallow water equations, we also model the total energy budget of the flow, by solving the following equation for the total mixture energy (sum of internal and kinetic energies):

$$\begin{aligned} \frac{\partial}{\partial t} \left[\rho_m h \left(C_v T + \frac{1}{2} (u^2 + v^2) \right) \right] + \frac{\partial}{\partial x} \left(\left[C_v T + \frac{1}{2} (u^2 + v^2) + g' \frac{h}{2} \right] \rho_m h u \right) \\ + \frac{\partial}{\partial y} \left(\left[C_v T + \frac{1}{2} (u^2 + v^2) + g' \frac{h}{2} \right] \rho_m h v \right) = -\rho_m g' h \left(u \frac{\partial B}{\partial x} + v \frac{\partial B}{\partial y} \right) \\ - \frac{1}{2} (u^2 + v^2) \sum_{i_s=1}^{n_s} (\rho_{s,i_s} D_{s,i_s}) - \sum_{i_s=1}^{n_s} (\rho_{s,i_s} C_{s,i_s} T D_{s,i_s}) + C_a \rho_a T_a E_a + C_{wv} \rho_{wv}^b T_b E_{wv}. \end{aligned} \quad (5)$$

where C_v is the mass averaged specific heat of the mixture, C_{s,i_s} , C_a and C_{wv} are the specific heat of solid, air and water vapour, respectively, and T_a and T_b are the atmospheric air and water vapour temperatures before entrainment. In this equation, heat transfer by thermal conduction is neglected, as well as thermal radiation. The full derivation of the energy equation is presented in Appendix A2.

It is worth noting that the design of conservative and stable numerical schemes for the solution of Eqs. (2-5) requires some care. This is because the numerical solution of mass and momentum equations, even when these quantities are globally conserved, does not necessarily result in an accurate description of the mechanical energy balance of the shallow water system (Fjordholm et al., 2011; Murillo and García-Navarro, 2013). This can lead to numerical errors associated with the mixture temperature obtained from the total mixture specific energy and the kinetic energy computed from mass and momentum equations. For this reason, in some cases, instead of the full energy equation as presented above, it is preferable to solve a simpler transport equation for the specific thermal energy $C_v T$:

$$\begin{aligned} \frac{\partial}{\partial t} (\rho_m h C_v T) + \frac{\partial}{\partial x} (C_v T \rho_m h u) + \frac{\partial}{\partial y} (C_v T \rho_m h v) = \\ - \sum_{i_s=1}^{n_s} (\rho_{s,i_s} C_{s,i_s} T D_{s,i_s}) + C_a \rho_a T_a E_a + C_{wv} \rho_{wv}^b T_b E_{wv}, \end{aligned} \quad (6)$$

We remark that in this equation we neglect heating associated with friction forces. This term can be important for some applications where viscous forces are particularly large, for example lava flows, but are negligible for the applications presented



in this work. It is also worth noting that the numerical solution of Eqs. (2-4,6) does not guarantee that the total energy is conserved. In the following, for simplicity, we use the temperature equation to demonstrate the writing of the system of equations in a more compact form and in the description of the numerical schemes.

Additional transport equations for the mass of n_s solid classes and the water vapour are also considered:

$$155 \quad \frac{\partial \alpha_{s,i_s} \rho_{s,i_s} h}{\partial t} + \frac{\partial (\alpha_{s,i_s} \rho_{s,i_s} h u)}{\partial x} + \frac{\partial (\alpha_{s,i_s} \rho_{s,i_s} h v)}{\partial y} = -\rho_{s,i_s} D_{s,i_s}, \quad i_s = 1, \dots, n_s \quad (7)$$

$$\frac{\partial \alpha_{wv} \rho_{wv} h}{\partial t} + \frac{\partial (\alpha_{wv} \rho_{wv} h u)}{\partial x} + \frac{\partial (\alpha_{wv} \rho_{wv} h v)}{\partial y} = \rho_{wv}^b E_{wv} \quad (8)$$

Introducing the vector of conservative variables

$$\mathbf{Q} = (Q_1, \dots, Q_{5+n_s})^T = \begin{bmatrix} \rho_m h \\ \rho_m h u \\ \rho_m h v \\ \rho_m h C_v T \\ \rho_{s_1} \alpha_{s_1} h \\ \vdots \\ \rho_{s_n} \alpha_{s_n} h \\ \rho_{wv} \alpha_{wv} h \end{bmatrix}. \quad (9)$$

it is possible to write the transport equations in the compact form:

$$160 \quad \mathbf{Q}_t + \mathbf{F}(\mathbf{Q})_x + \mathbf{G}(\mathbf{Q})_y = \mathbf{S}_1(\mathbf{Q}) + \mathbf{S}_2(\mathbf{Q}) + \mathbf{S}_3(\mathbf{Q}), \quad (10)$$

where the fluxes \mathbf{F} and \mathbf{Q} are

$$\mathbf{F}(\mathbf{Q}) = \begin{bmatrix} \rho_m h u \\ \rho_m h u^2 + \rho_m g' \frac{h^2}{2} \\ \rho_m h u v \\ C_v T \rho_m h u \\ \alpha_{s,1} \rho_{s,1} h u \\ \vdots \\ \alpha_{s,n} \rho_{s,n} h u \\ \alpha_{wv} \rho_{wv} h u \end{bmatrix}, \quad \mathbf{G}(\mathbf{Q}) = \begin{bmatrix} \rho_m h v \\ \rho_m h u v \\ \rho_m h v^2 + \rho_m g' \frac{h^2}{2} \\ C_v \rho_m h v \\ \alpha_{s,1} \rho_{s,1} h v \\ \vdots \\ \alpha_{s,n} \rho_{s,n} h v \\ \alpha_{wv} \rho_{wv} h v \end{bmatrix}, \quad (11)$$



the source terms \mathbf{S}_1 and \mathbf{S}_2 associated with the topography/gravitational and friction forces are

$$\mathbf{S}_1(\mathbf{Q}) = \begin{bmatrix} 0 \\ -\rho_m g' h \frac{\partial B}{\partial x} \\ -\rho_m g' h \frac{\partial B}{\partial y} \\ 0 \\ 0 \\ \vdots \\ 0 \end{bmatrix}, \quad \mathbf{S}_2(\mathbf{Q}) = \begin{bmatrix} 0 \\ F_x \\ F_y \\ 0 \\ 0 \\ \vdots \\ 0 \end{bmatrix} \quad (12)$$

165 and the source term \mathbf{S}_3 associated with deposition and entrainment is

$$\mathbf{S}_3(\mathbf{Q}) = \begin{bmatrix} -\sum_{i_s=1}^{n_s} [\rho_{s,i_s} D_{s,i_s}] + \rho_a E_a + \rho_{wv} E_{wv} \\ -u \sum_{i_s=1}^{n_s} (\rho_{s,i_s} D_{s,i_s}) \\ -v \sum_{i_s=1}^{n_s} (\rho_{s,i_s} D_{s,i_s}) \\ -\sum_{i_s=1}^{n_s} (\rho_{s,i_s} C_{s,i_s} T D_{s,i_s}) + C_a \rho_a T_a E_a \\ -\rho_{s,1} D_{s,1} \\ \vdots \\ -\rho_{s,n} D_{s,n} \\ \rho_{wv} E_{wv} \end{bmatrix}. \quad (13)$$

Finally, the following equation describes the temporal evolution of the topography:

$$\frac{\partial B}{\partial t} = \sum_{i_s=1}^{n_s} D_{s,i_s}. \quad (14)$$

170 The model described by the equations above generalize that presented by de' Michieli Vitturi et al. (2019) for granular flows, where the mixture was treated as a single-phase granular fluid. In fact, by neglecting deposition and entrainment terms and the equation for water-vapour, the gas-particle mixture behaves as a homogeneous phase with constant density and temperature. In addition, if we use the Voellmy-Salm friction rheology, the system of equations becomes equivalent to that presented in de' Michieli Vitturi et al. (2019).

175 It is important to remark that here, in comparison to Shimizu et al. (2017b, 2019), we do not enforce a front condition for the propagating flow, in terms of front velocity or Freude number. As described in Marino et al. (2005), this condition applies to channelized flows for a phase during which, after an initial acceleration (as for lock-exchange experiments), the velocity of the front becomes constant (then followed by a front deceleration). The code we present is mostly aimed at simulating 2D spreading flows, for which we do not simulate the initial phase and, most importantly, for which the front velocity decreases because of the radial spread. An alternative approach, which allows correct simulation of the behavior of shocks without
 180 additional closure relations for the front, has been proposed in Fyhn et al. (2019). This approach relies on a formulation of the momentum equation in a non-conservative form, but at present is applicable for 1D shallow water equations only, and further



studies are needed to adapt it to the 2D formulation. The application of modified finite-volume central-upwind schemes for non-conservative terms, as those proposed in Diaz et al. (2019), could provide a reliable framework for the implementation in IMEX-SfloW2D of the approach described in Fyhn et al. (2019), in order to better simulate the constant velocity phase of channelized flows.

3 Constitutive equations for dilute turbulent currents

The system of conservation equations (10) represents the set of partial differential equations governing the transient dynamics of the multiphase flow of interest, but their physical and mathematical description is not complete without some closure relations describing the properties of the flow (density, deposition, entrainment, friction) as functions of the conservative or primitive variables. These relations are called constitutive equations, and they characterize the different flows we can solve with the model. In particular, in this section we describe the constitutive equations used to model dilute turbulent gas-particle currents. It is important to remark that, with appropriate choice of the friction terms and the constitutive equations, the model can be applied to a wider range of geophysical flows such as pyroclastic avalanches or lahars.

3.1 Gas density

Density of air and water vapour are computed using the ideal gas law, expressed as a function of temperature and pressure:

$$\rho_a = \frac{P}{R_{sp,a}T}, \quad \rho_{wv} = \frac{P}{R_{sp,wv}T}. \quad (15)$$

Here, P is the ambient pressure (Pa) and $R_{sp,a}$ and $R_{sp,wv}$ are the specific gas constant for dry air and water vapour, respectively. We remark that we assume that density does not change with changes in hydrostatic pressure within the flow, but only with changes in flow temperature (Bursik and Woods, 1996; Shimizu et al., 2019).

3.2 Mixture density

Mixture density has already been introduced in Section 2 and it is given by Eq. 1.

3.3 Air entrainment

In large scale natural flows, entrainment of ambient fluid into a gravity current can be significant, diluting the flow to the point where it can become buoyant. As the flow propagates, air is entrained at a rate which: (i) is proportional to the magnitude of the difference in velocity between the flow and the stationary ambient; and (ii) depends on the ratio of the stabilizing stratification of the current to destabilizing velocity shear. This ratio is expressed by the Richardson number $Ri = g'h/(u^2 + v^2)$, where g' is the reduced gravity. Thus, following Morton et al. (1956), we take the volumetric rate of entrainment of ambient air into the flow due to turbulent mixing as:

$$E_a = \epsilon \sqrt{(u^2 + v^2)} \quad (16)$$



210 where ϵ is the entrainment coefficient given by

$$\epsilon = \frac{0.075}{(1 + 718 Ri^{2.4})^{0.5}}. \quad (17)$$

The Richardson number is important not only for the entrainment of ambient air, but also because the value $Ri = 1$ represents a critical threshold between subcritical ($Ri > 1$) and supercritical ($Ri < 1$) regimes, i.e. between a regime where flow velocity is slower than the speed with which gravity waves propagate (wave celerity) and a velocity where flow velocity is faster than wave celerity. Thus, the Richardson number is important also when boundary conditions are prescribed. We remark that at an inlet it is not possible to prescribe all the flow variables for subcritical flows, because the dynamics are also controlled by downstream conditions.

3.4 Water vapour entrainment

The entrainment of water vapour resulting from the interaction of the flows with water is modeled following the ideas presented in Dufek et al. (2007). A series of experiments have shown that the amount of heat transfer is governed by the rate of particle deposition onto the water surface. At the water surface, steam is produced around the particles and ingested into the flow, but as particles sink deeper into the water, the steam produced condenses and is no longer available to be ingested into the flow. Thus, only a fraction of the thermal energy lost by the particles deposited by the flow over water contributes to the "effective" steam production. The coefficients $\gamma_{i_s, wv}$ represent the fraction of thermal energy from the particles of class i_s lost by the flow which results in the production of water vapour entrained in the flow. Thus, it is null when the current travels over land and between 0 and 1 when the current travels over water. As a first order approximation, 10% of the thermal energy of the particles is partitioned and is available to produce steam ($\gamma_{i_s, wv} = 0.1$), and smaller particles have greater steam production rates ($\gamma_{i_s, wv} > 0.1$).

The rate of water vapour production associated with this process is obtained with a balance of the rate of thermal energy lost by the particles and that necessary to produce the steam:

$$\rho_{wv}^b E_{wv} [C_l(T_b - T_l) + L_w] = \sum_{i_s=1}^{n_s} \gamma_{i_s, wv} (\rho_{s, i_s} C_{s, i_s} T D_{s, i_s}) \quad (18)$$

where ρ_{wv}^b is the density of water vapour at boiling point, C_l is the specific heat of liquid water, T_l is the temperature of water, T_b is the boiling temperature, and L_w is the latent heat of vaporization.

3.5 Sedimentation

Sedimentation of particles from the flow is modeled as a mass flux at the flow bottom and is assumed to occur at a rate which is proportional to the particle settling velocity v_s , to the bulk density of particles in the flow and to a factor depending on the total solid volume fraction (Bürger and Wendland, 2001), accounting for hindered settling phenomena:

$$D_s = \alpha_s \cdot v_s(d_s) \left(1 - \frac{\sum \alpha_s}{\alpha_{max}}\right)^n \quad n > 1 \quad (19)$$



where α_{max} is the maximum volume fraction of solids, which generally occurs at fractions between 0.6 and 0.7, while n is an
 240 empirical exponent (4.65 is a suitable value for rigid spheres).

The particle settling velocity v_s is a function of the particle diameter d_s , and is given by the following non-linear equation:

$$v_s^2(d_s)C_D(Re) = \frac{4}{3}d_s g \left(\frac{\rho_s - \rho_a}{\rho_a} \right). \quad (20)$$

The gas-particle drag coefficient $C_D(Re)$ is given by the following relations, as a function of the Reynolds number $Re = \frac{d_s v_s}{\nu}$
 (Lun and Gidaspow, 1994):

$$\begin{aligned} 245 \quad Re > 1000; \quad C_D(Re) &= 0.44 \\ Re \leq 1000; \quad C_D(Re) &= \frac{24}{Re} (1 + 0.15Re^{0.687}) \end{aligned}$$

and ν is the kinematic viscosity coefficient of atmospheric air.

Eq. 20 has an analytical solution in the limit of coarse particles ($Re > 1000$), :

$$v_s(d_s) = \sqrt{\frac{4}{3C_D} \left(\frac{\rho_s - \rho_a}{\rho_a} \right) d_s g}, \quad (21)$$

250 and in the limit of very fine particles ($Re \ll 1$):

$$v_s(d_s) = \frac{d_s^2}{18\nu} \left(\frac{\rho_s - \rho_a}{\rho_a} \right) g. \quad (22)$$

In the intermediate regimes, Eq. 20 is solved numerically.

3.6 Friction model

Several friction models have been implemented in the numerical code. For the applications presented in this work, a simple
 255 model has been used, with the force being proportional to the square of flow velocity through a basal friction coefficient f
 depending on terrain roughness:

$$\mathbf{F} = (F_x, F_y) = -f\rho_m \sqrt{(u^2 + v^2)}(u, v). \quad (23)$$

The friction factor typically has a value in the range 0.001-0.02 (Bursik and Woods, 1996). This form is equivalent to the
 Voellmy-Salm model (Bartelt et al., 1999) when the contribution of the basal Coulomb friction is neglected.

260 4 Numerical discretization

In this section we present the details of the numerical scheme implemented to solve the system of equations (10). It is important
 to remark that different processes contributing to the dynamics of the flows of interest have different time scales, and thus they
 require different numerical techniques. For this reason, a splitting approach is adopted in the code to integrate separately: (i)
 the advective, gravitational and frictional terms; and (ii) the deposition and entrainment terms.



265 The numerical solver for the solution of Eq. (10) (without the deposition and entrainment terms represented by \mathbf{S}_3) is based, as in de' Michieli Vitturi et al. (2019), on an IMEX Runge-Kutta scheme, where the conservative fluxes \mathbf{F} and \mathbf{G} and the terms \mathbf{S}_1 are treated explicitly, while the stiff terms of the equations, represented by \mathbf{S}_2 , are discretized implicitly (Pareschi and Russo, 2005). The use of an implicit scheme for friction terms allows for larger time steps and to properly model conditions such as initiation and cessation phases, without the need for empirical thresholds on the velocity or thickness of the flow. For
 270 the spatial discretization of the fluxes, as in the first version of the code, we adopt a central-upwind finite-volume method (Kurganov et al., 2001; Kurganov and Petrova, 2007; de' Michieli Vitturi et al., 2019; Biagioli et al., 2021) on co-located grids derived from DEMs in UTM coordinates, thus on uniform grids of equally sized square pixels. The central-upwind approach guarantees an accurate description of the propagation of the dry/wet interface (front of the flow) and the positivity of the solution.

275 We denote the vector of discretized values of the conservative variables with $\mathbf{Q}_{j,k}$, where the first index refers to the longitude and the second to the latitude. These values represent the average value of the conservative variables on each computational cell and are associated to the cell centers (see Figure 1). Similarly, the discretized values of the topography elevation $\mathbf{B}_{j,k}$ are saved at the cell centers. We also use the superscripts E , W , N , and S to denote the east, west, north and south values of the variables inside a cell. Discontinuities are allowed for in the numerical solution at the cell interfaces. In fact, at the interface
 280 $(j + \frac{1}{2}, k)$ we can have two distinct values of the numerical solutions, $\mathbf{Q}_{j,k}^E$ and $\mathbf{Q}_{j+1,k}^W$ (see Figure 1). This is true also for the discretized topography. From the set of conservative variables \mathbf{Q} , a second set of variables, which we will call *primitive variables*, is derived:

$$\mathbf{P} = (h, hu, hv, T, h\alpha_{s,1}, \dots, h\alpha_{s,n_s}, h\alpha_{wv}, u, v) \quad (24)$$

The full derivation of the primitive variables from the conservative variables is presented in the Appendix. We remark that,
 285 following Kurganov and Petrova (2007), when the velocities u and v are computed from the conservative variables $Q_2 = \rho_m hu$ and $Q_3 = \rho_m hv$, a desingularization is applied to avoid large velocities that might arise because of the division by very small values of thickness, as it could occur close to the flow front.

From the values of the primitive variables $\mathbf{P}_{j,k}$ at the cell centers, the partial derivatives $(\mathbf{P}_x)_{j,k}$ and $(\mathbf{P}_y)_{j,k}$ are computed, using opportune slope limiters (MinMod, Superbee or Van Leer). Then, the values at the internal sides of each cell interface
 290 are reconstructed with a linear interpolation from the cell center values:

$$\begin{aligned} \mathbf{P}_{j,k}^E &= \mathbf{P}_{j,k} + \frac{\Delta x}{2} (\mathbf{P}_x)_{j,k}, & \mathbf{P}_{j,k}^W &= \mathbf{P}_{j,k} - \frac{\Delta x}{2} (\mathbf{P}_x)_{j,k}, \\ \mathbf{P}_{j,k}^N &= \mathbf{P}_{j,k} + \frac{\Delta y}{2} (\mathbf{P}_y)_{j,k}, & \mathbf{P}_{j,k}^S &= \mathbf{P}_{j,k} - \frac{\Delta y}{2} (\mathbf{P}_y)_{j,k}. \end{aligned}$$

This choice for primitive variables allows prescription of the boundary conditions at the cell interfaces in a natural way, because usually they are given in terms of flow thickness, volumetric flow rate, phases fractions and temperature, or in terms
 295 of their gradient.

Once the primitive variables at the interfaces are known (either from the reconstruction or from the boundary conditions at the boundary cells), we compute the corresponding conservative variables $\mathbf{Q}_{j,k}^E$, $\mathbf{Q}_{j,k}^W$, $\mathbf{Q}_{j,k}^N$ and $\mathbf{Q}_{j,k}^S$. Primitive and conservative

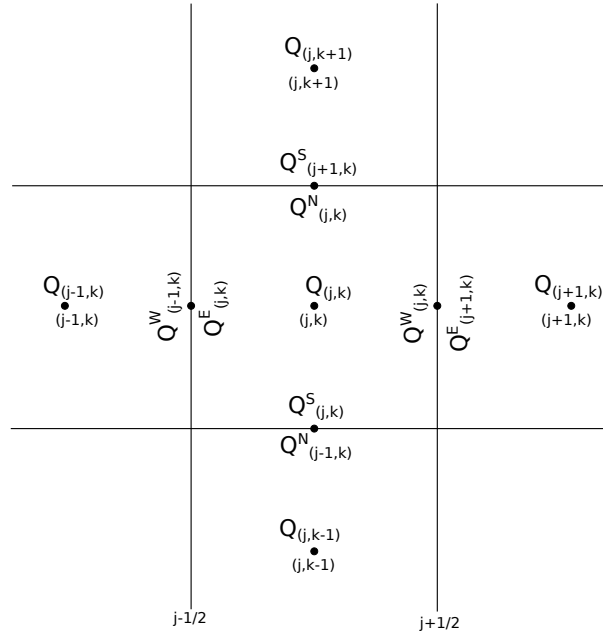


Figure 1. Sketch of the numerical grid and conservative variables indexing. The average value of the vector of conservative variables on each computational cell is denoted by $\mathbf{Q}_{j,k}$ and is associated to the cell center. The vectors $\mathbf{Q}_{j,k}^E$, $\mathbf{Q}_{j,k}^W$, $\mathbf{Q}_{j,k}^N$ and $\mathbf{Q}_{j,k}^S$ are defined at the cell interfaces and represents the interface values of the conservative variables. At each interface two interface vectors are defined.

variables are then used to compute the fluxes $\mathbf{F}(\mathbf{P}_{j,k}^{(\cdot)}, \mathbf{Q}_{j,k}^{(\cdot)})$ and $\mathbf{G}(\mathbf{P}_{j,k}^{(\cdot)}, \mathbf{Q}_{j,k}^{(\cdot)})$ at the sides of the interfaces. We observe that the set of primitive variables is redundant, but this redundancy allows us to obtain a stable numerical scheme. In particular, for the
 300 advective flux terms, the advection velocity components are obtained from the primitive variables, while the variables to advect are taken directly from the conservative variables. The use of this combination of reconstructed primitive and conservative variables for the calculation of the fluxes, together with the application of limiters, makes the numerical scheme stable, avoiding the origin of large values of thickness and velocity. The fluxes at the two sides of each interface are then used to compute the numerical fluxes.

305 Following Kurganov and Petrova (2007), the numerical fluxes in the x -direction are given by:

$$\mathbf{H}_{j+\frac{1}{2},k}^x = \frac{a_{j+\frac{1}{2},k}^+ \mathbf{F}(\mathbf{P}_{j,k}^E, \mathbf{Q}_{j,k}^E) - a_{j+\frac{1}{2},k}^- \mathbf{F}(\mathbf{P}_{j+1,k}^W, \mathbf{Q}_{j+1,k}^W)}{a_{j+\frac{1}{2},k}^+ - a_{j+\frac{1}{2},k}^-} + \frac{a_{j+\frac{1}{2},k}^+ a_{j+\frac{1}{2},k}^-}{a_{j+\frac{1}{2},k}^+ - a_{j+\frac{1}{2},k}^-} (\mathbf{Q}_{j+1,k}^W - \mathbf{Q}_{j,k}^E) \quad (25)$$



where the right- and left-going local speeds $a_{j+\frac{1}{2},k}^+$ and $a_{j+\frac{1}{2},k}^-$ are estimated by:

$$310 \quad \begin{aligned} a_{j+\frac{1}{2},k}^+ &= \max\left(u_{j,k}^E + \sqrt{g'h_{j,k}^E}, u_{j+1,k}^W + \sqrt{g'h_{j+1,k}^W}, 0\right), \\ a_{j+\frac{1}{2},k}^- &= \min\left(u_{j,k}^E - \sqrt{g'h_{j,k}^E}, u_{j+1,k}^W - \sqrt{g'h_{j+1,k}^W}, 0\right). \end{aligned}$$

It is important here to remark that we have two local speeds not because they are associated to the two different sides of each interface, but because one is for the left-going characteristic speeds (on both sides) and the other for the right-going speeds (on both sides).

In a similar way, the numerical fluxes in the y -direction are given by:

$$315 \quad \mathbf{H}_{j,k+\frac{1}{2}}^y = \frac{b_{j,k+\frac{1}{2}}^+ \mathbf{G}(\mathbf{P}_{j,k}^N, \mathbf{Q}_{j,k}^N) - b_{j,k+\frac{1}{2}}^- \mathbf{G}(\mathbf{P}_{j+1,k}^S, \mathbf{Q}_{j+1,k}^S)}{b_{j,k+\frac{1}{2}}^+ - b_{j,k+\frac{1}{2}}^-} + \frac{b_{j,k+\frac{1}{2}}^+ b_{j,k+\frac{1}{2}}^-}{b_{j,k+\frac{1}{2}}^+ - b_{j,k+\frac{1}{2}}^-} (\mathbf{Q}_{j+1,k}^S - \mathbf{Q}_{j,k}^N) \quad (26)$$

where the local speeds in the y -direction $b_{j+\frac{1}{2},k}^+$ and $b_{j+\frac{1}{2},k}^-$ are given by:

$$\begin{aligned} b_{j,k+\frac{1}{2}}^+ &= \max\left(v_{j,k}^N + \sqrt{g'h_{j,k}^N}, v_{j,k+1}^S + \sqrt{g'h_{j,k+1}^S}, 0\right), \\ b_{j,k+\frac{1}{2}}^- &= \min\left(v_{j,k}^N - \sqrt{g'h_{j,k}^N}, v_{j,k+1}^S - \sqrt{g'h_{j,k+1}^S}, 0\right). \end{aligned}$$

320 The explicit computation of the term \mathbf{S}_1 requires the numerical discretization of the spatial gradient of the topography. The partial derivatives $(B_x)_{j,k}$ and $(B_y)_{j,k}$ are computed from the cell averages using the same slope limiter used for h . Then, the topography is computed at the interfaces with a linear reconstruction, obtaining for each cell the values:

$$\begin{aligned} \mathbf{B}_{j,k}^E &= \mathbf{B}_{j,k} + \frac{\Delta x}{2} (\mathbf{B}_x)_{j,k}, & \mathbf{B}_{j,k}^W &= \mathbf{B}_{j,k} - \frac{\Delta x}{2} (\mathbf{B}_x)_{j,k}, \\ \mathbf{B}_{j,k}^N &= \mathbf{B}_{j,k} + \frac{\Delta y}{2} (\mathbf{B}_y)_{j,k}, & \mathbf{B}_{j,k}^S &= \mathbf{B}_{j,k} - \frac{\Delta y}{2} (\mathbf{B}_y)_{j,k}. \end{aligned}$$

325 The implicit part of the IMEX Runge-Kutta scheme, associated with the integration of the friction terms, is solved using a Newton-Raphson method with an optimum step size control, where the Jacobian of the implicit terms is computed with a complex-step derivative approximation (de' Michieli Vitturi et al., 2019).

After each Runge-Kutta procedure, the deposition and air entrainment term are computed explicitly and the flow variables and the topography at the centers of the computational cells are updated.

330 For large time steps, the explicit treatment of solid deposition could lead to negative solid volumetric fractions in the flow, and for this reason the effective deposition rate \overline{D}_{s,i_s} is limited at each integration step in order to prevent this occurrence:

$$\overline{D}_{s,i_s} = \min[D_{s,i_s}, \Delta t \cdot (\alpha_{s,i_s} h)].$$

The use of an explicit integration scheme for the terms of the equations containing spatial derivatives, with respect to an implicit treatment, has the advantage that the solutions of the discretized equations in each cell are decoupled, without the need



335 to solve for a large linear system. The same is true for the integration of the friction, deposition and entrainment terms. This allowed implementation of a parallel strategy to advance in time the numerical solution of the discretized equations, requiring almost no communication or dependency between the processes. Thus, with a small effort, the Fortran implementation of the code has been updated by parallelizing all the loops over the computational cells with the Open MultiProcessor (OpenMP) programming model for shared-memory platforms.

340 The schemes implemented for the numerical discretization of the governing equations do not depend on the particular choice of the constitutive equation or on the friction force, thus they apply also when the model is used to solve for different volcanic mass flows.

5 Numerical benchmarks

In this section we present applications of the model to 1D and 2D problems. They add to numerical benchmarks and validation tests previously presented by (de' Michieli Vitturi et al., 2019). The 1D benchmark tests are designed to demonstrate the capability of the numerical scheme to describe the interaction of the flow of obstacles in different regimes (subcritical, supercritical, transitional). Then, model results are compared with those presented in (Engwell et al., 2016) for large ash flows, to compare the steady state produced by our 2D transient simulations with that obtained with a 1D axisymmetric steady-state model.

5.1 One dimensional subcritical and transcritical flows

350 When dealing with flows where velocity and mixture density can experience large changes, it is important to have a model which properly describes both subcritical ($Ri > 1$) and supercritical ($Ri < 1$) regimes and the transition between them. In the subcritical regime, flow is dominated by gravitational forces, with greater thickness and lower velocities; for supercritical flow it is the opposite, with thinner and faster flow dominated by inertial forces. In addition, it is fundamental to have a model that is able to describe accurately how the flow interacts with the topography under these different regimes. As shown in Woods et al. (1998) using both laboratory experiments and theoretical models, when a flow interacts with a topographic barrier such as a ridge, the flow thickness and velocity can change in different ways depending on the height of the ridge and the flow speed (Houghton and Kasahara, 1968). Under some circumstances, flows may be partially blocked and producing upstream propagating bores resulting in increased sedimentation upstream of the barrier. In other cases, the flow is able to overcome the ridge, but with a transition in flow regime, and thus in the sedimentation pattern.

360 Here, we present some numerical simulations reproducing literature benchmarks and showing the capability of the numerical code to properly model the subcritical and supercritical regimes, and the transition between them. Following Goutal (1997); Delestre et al. (2013); Michel-Dansac et al. (2016), we simulate a steady one-dimensional flow in a 25 m domain with a parabolic bump on the bottom, where the topography is given by

$$B(x) = \begin{cases} 0.2 - 0.05(x - 10)^2 & 8 < x < 12 \\ 0 & elsewhere \end{cases} \quad (27)$$



365 The flow travels in the x -direction ($u > 0$ m/s, $v = 0$ m/s), with constant density (for simplicity $\rho = 1$ kgm⁻³) and constant temperature (energy equation is not needed). Furthermore, no friction, mass entrainment and deposition are considered for the test cases presented in this section. With these assumptions, in the steady state regime, we can derive from Eqs. (2-3) the following simpler governing equations:

$$\begin{cases} \frac{\partial(hu)}{\partial x} = 0 \\ \frac{\partial}{\partial x} \left(hu^2 + \frac{1}{2}g'h^2 \right) = -g'h \frac{\partial B}{\partial x} \end{cases} \quad (28)$$

370 By expanding the derivative on the left-hand side of the momentum equation, we obtain:

$$u \frac{\partial u}{\partial x} + g' \frac{\partial h}{\partial x} = g' \frac{\partial B}{\partial x} \quad (29)$$

and, by substituting the expression of $\partial u / \partial x$ computed from the mass equation, we have

$$\left(1 - \frac{u^2}{g'h} \right) \frac{\partial h}{\partial x} = - \frac{\partial B}{\partial x} \quad (30)$$

which, written in terms of the Richardson number Ri , gives

$$375 \left(1 - \frac{1}{Ri} \right) \frac{\partial h}{\partial x} = - \frac{\partial B}{\partial x} \quad \text{or} \quad (1 - Ri) \frac{\partial}{\partial x} (h + B) = \frac{\partial B}{\partial x}. \quad (31)$$

According to these equations, the subcritical or supercritical regime determines whether flow thickness h and free surface $h + B$ increases or decreases as the fluid interacts with the topography. It is also important to observe that in supercritical flows ($Ri < 1$), upstream conditions fully determine the flow immediately downstream, while in subcritical flows changes in downstream conditions affect the flow upstream. From a numerical point of view, this is important when prescribing flow
 380 boundary conditions, because we can only prescribe all flow variables at the inlet for supercritical flows. We remark here that the test cases presented in this section are not meant to be representative of real dilute PDCs conditions, but they have been chosen to show the capability of the numerical model to properly simulate different flow regimes and their transitions.

The first test case is a flow where at the left boundary of the domain an influx with $h = 1$ m and $u = 10$ m s⁻¹ is prescribed, resulting in a supercritical regime ($Ri < 10^{-2}$). As previously stated, the supercritical conditions at the inlet are consistent with
 385 the two boundary conditions assigned. For this simulation, as for the other simulations presented in this section, the domain is partitioned with 1000 uniform cells, and a linear reconstruction of the primitive variables with a minmod limiter has been used. For this supercritical test, the solution at $t = 0$ is initialized with a constant thickness corresponding to the inlet value and with zero velocity. The solution at $t = 120$ s, when a steady state is reached, is presented in terms of the flow free surface (Fig. 2a, orange line) and flow velocity (Fig. 2b). In this supercritical condition, the fluid thickens and slows as it passes over the
 390 top of the obstacle, reaching its minimum speed at the crest ($x = 10$ m). The slope of the free surface follows the slope of the obstacle, increasing before the crest and then decreasing in elevation. The higher the Richardson number, the smaller the effect of topography on flow thickness and on velocity, with the free surface mimicking the slope of the topography.

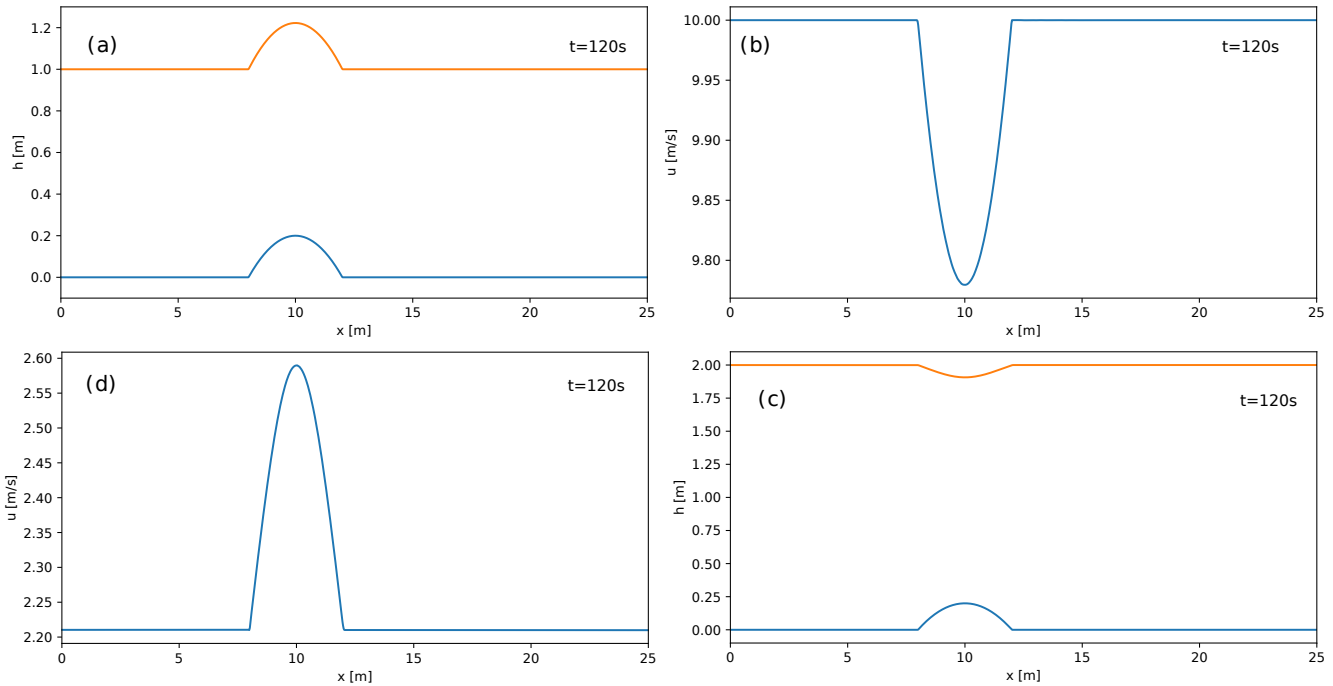


Figure 2. Thickness (left) and velocity (right) profiles in one-dimensional flows over a bump. Steady solutions for supercritical and subcritical flows are shown in top and bottom panels, respectively.

The second test case is a simulation of a subcritical regime. In this case an influx of $4.42 \text{ m}^2 \text{ s}^{-1}$ is prescribed at the left boundary, while a flow thickness of 2 m is fixed at the outlet. It is important to observe that here, in contrast to the previous case, we cannot prescribe both flow thickness and velocity at the inlet, because of the subcritical condition. Also for this case, the solution in the domain is initialized at $t = 0 \text{ s}$ with a constant thickness corresponding to the outlet value and with zero velocity. The numerical solution at $t = 120 \text{ s}$, corresponding to a steady state, is presented in the bottom panel of Fig. 2. In this case, the fluid thins and accelerates as it crosses the top of the obstacle, reaching its maximum speed and minimum thickness at the crest. Accordingly with the second of Eqs. (31), the free surface also decreases where the bottom slope is positive, while it increases after reaching the bottom crest.

The interaction of a flow with an obstacle can also lead to a transition in the flow regime (transcritical flow). If the flow is subcritical upstream and it undergoes a sufficient increase in velocity and decrease in thickness as it ascends toward the crest, a smooth transition from subcritical to supercritical flow can occur. This transition is shown in the top panels of Fig. 3, representing the flow free surface at $t = 120 \text{ s}$ for a flow with an influx of $1.53 \text{ m}^2 \text{ s}^{-1}$ prescribed at the left boundary and a thickness of 0.66 m fixed at the outlet, when the flow is subcritical. In fact, when the flow becomes supercritical, no boundary condition can be prescribed at the outlet, and the outlet thickness is an outcome of the simulation (here $h = 0.4 \text{ m}$). For this simulation, the solution in the domain is initialized at $t = 0 \text{ s}$ with a constant free surface corresponding to the outlet subcritical

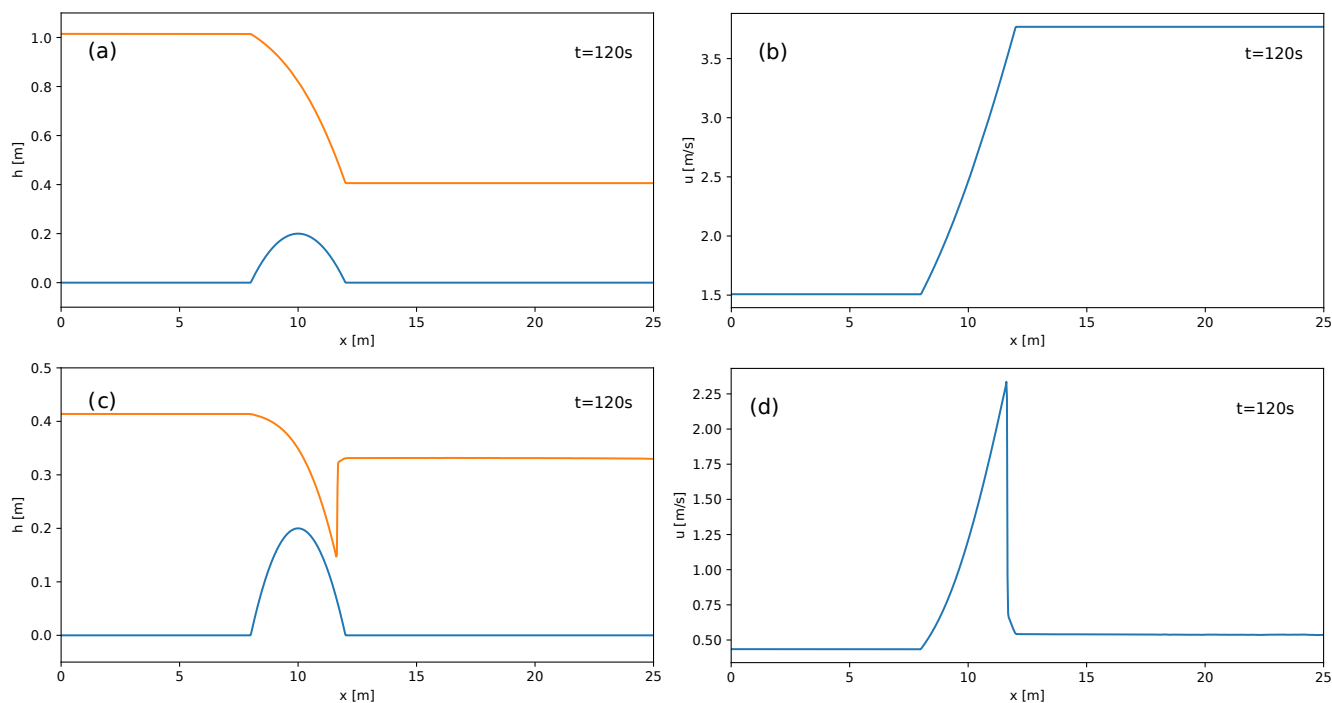


Figure 3. Flow thickness (left) and velocity (right) profiles in one-dimensional flows over a bump. Steady solutions for transcritical flows without and with shock are shown in top and bottom panels, respectively.

value and with zero velocity. Under certain conditions the flow, after an initial thinning and acceleration over the obstacle, can suddenly thicken and decelerate in correspondence with a flow regime transition. This transition from a rapid, supercritical flow to a slow, subcritical flow, called a hydraulic jump, is shown in Fig. 3, bottom panel, representing the flow free surface at $t = 120$ s for a flow with an influx of $0.18 \text{ m}^2 \text{ s}^{-1}$ prescribed at the left boundary and a thickness of 0.33 m fixed at the outlet. The steady state conditions obtained for these transonic (with and without shock) test cases are similar to that obtained in laboratory experiments presented in Fig. 4a of Woods et al. (1998), which showed that the deposit is weakly affected by the presence of the ridge and the regime transition.



415 In addition to the literature test-cases described above, aimed at reproducing steady-state flows for different regimes, we
present here another test case showing the temporal evolution of a flow with a steady inlet condition, where the interaction
with an obstacle results in the transition from subcritical to supercritical regime, and the backward propagation of a hydraulic
jump. The boundary conditions (inlet and outlet) are based on the configurations described in Khezri (2014) and Putra et al.
(2019) and, as for the previous tests, we assume a constant density ($\rho = 1 \text{ kg m}^{-3}$) and neglect friction, mass entrainment and
420 deposition. The computational domain is 10 m long (discretized with 1000 cells) and the inlet flow velocity and thickness are
fixed to 0.74 m s^{-1} and 0.14 m, respectively. The same values are used for the initial conditions up to 8 m from the inlet,
while no flow is present beyond this distance. At a distance of 9m from the inlet, a 0.1 m high wall is present, represented by a
discontinuity in the topography:

$$B(x) = \begin{cases} 0 & x \leq 9 \text{ m}, \\ 0.1 & x > 9 \text{ m} \end{cases} . \quad (32)$$

425 Some snapshots of the first 40 s of the simulation are shown in 4, with the flow thickness on the left panels and the velocity
on the right panels. When the flow front reaches the wall, flow thickness increases and its velocity decreases, with a transition
from supercritical to subcritical regime. The transition zone propagates backward, similarly to a tidal bore. At the same time,
due to an increase in flow thickness, part of the flow overcomes the obstacle and propagates beyond it. This behavior is similar
to that illustrated in Woods et al. (1998), Fig. 9, for a large ash flow interacting with a ridge. While they interpreted the bore as a
430 reflected part of the flow, which can carry fine-grained material back upstream, the right panels of Fig. 4 show that flow velocity
is always positive. This means that, for the simulation presented here, the increase in flow thickness propagating upstream is
not due to a negative flow velocity or a flow reflection, but to the backward propagation of the hydraulic jump. At later stages
(not shown here) a steady state is reached, with the flow being subcritical before and supercritical after the wall. A similar
behaviour can be expected when a supercritical PDC reaches a sufficiently high topographic obstacle. This, because of the
435 transition to a subcritical regime, would result in an increased sedimentation rate before the obstacle.

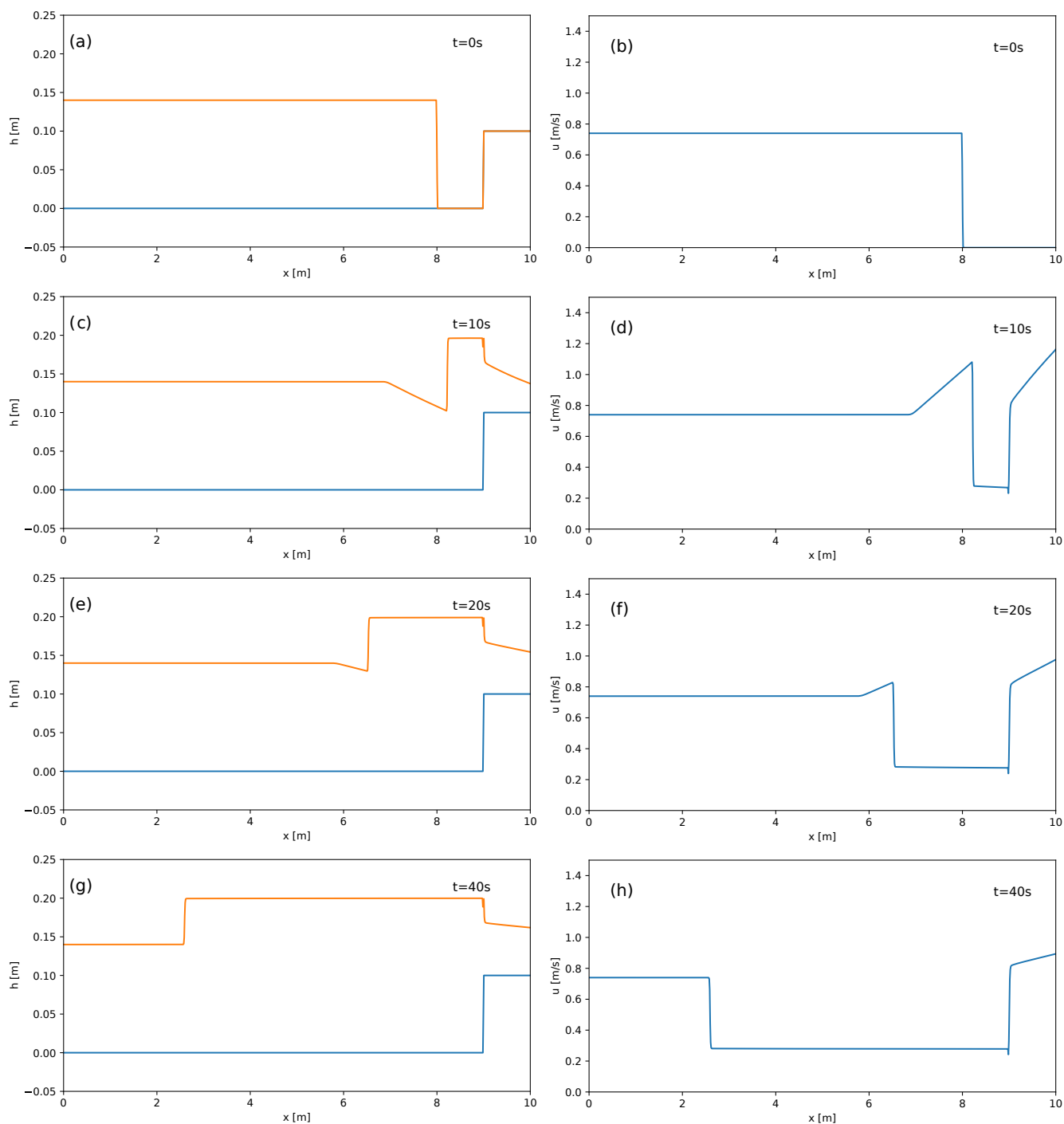


Figure 4. Thickness (left) and velocity (right) profiles for a one-dimensional subcritical flow with a backward propagating hydraulic jump.



5.2 Radial ash flow

In this section we apply the new model to reproduce results presented in Engwell et al. (2016) for large dilute flows producing coignimbrite columns. Thus, in comparison to the test cases of the previous section, we model a mixture of gas and solid particles, here with a diameter 100 microns. Solid deposition and atmospheric air entrainment are also modeled, resulting in
440 a mixture for which temperature and density change during the transport. Engwell et al. (2016) used a steady-state 1D model with radial symmetry, and here we want to reproduce the steady condition with transient 2D simulations. To be consistent with the assumptions of Engwell et al. (2016), and to obtain a steady state, we do not consider any modification of the topography associated with the deposition of solid particles. In this way, with a steady source, it is possible to reach a steady condition and a steady radial profile.

445 The use a steady-state numerical code, as done by Engwell et al. (2016), restricts the study to supercritical flows, and in this section we present numerical simulations for supercritical conditions only. As discussed for the previous example, subcritical and supercritical boundary conditions corresponds to two different physical settings, and different boundary/source conditions are prescribed to model the different initial regimes. In the supercritical regime, flow downstream from the source is controlled by conditions upstream, and all the conservative variables must be fixed at the boundary inlet. This is the case for the two
450 axisymmetric simulations presented in Fig. 5 and Fig. 6, where the initial Richardson numbers are 0.1 and 0.9, respectively. For both simulations the inlet conditions are given at $R = 2000$ m, with the initial thickness fixed at $h = 2000$ m, the initial gas mass fraction at 0.2, the initial temperature at $T = 900$ K and the friction coefficient at 0.001. The initial velocities are computed from the other variables and the Richardson number, resulting in an initial radial velocity of 93.32 m s^{-1} for $Ri = 0.9$ and 279.98 m s^{-1} for $Ri = 0.1$. A 20km by 20km computational domain, discretized with 100m size cells, is used for the two
455 simulations. For both simulations, when the mixture becomes buoyant in a computational cell (due to entrainment and heating of atmospheric air and particle sedimentation), the mass is removed from that cell, while the solution is not computed for the cells that are fully inside the area defined by $R < 2000$ m. The two figures show the flow solution at $t = 200$ s, when a steady condition for both radial flows is reached. In the left panels a 3D view of the flow thickness is presented. The color of the free surface represents flow thickness, clearly showing a lower thickness for the simulation with initial $Ri = 0.9$. When using
460 Cartesian grids to model axisymmetrical flows, it is not obvious that the output of the simulation would produce the correct results in terms of radial symmetry of the flow front. In fact, while the inlet velocity is given analytically at the lateral surface of the inlet cylinder, i.e. at a distance of 2000m from the point (0,0), the boundary conditions are prescribed numerically at the faces of the computational cells, which can be at different distances. For this reason, a correction on the velocity accounting for this discrepancy is applied to each inlet face. Model results, as shown in the left panels, highlight that this correction, coupled
465 with the second-order discretization in space implemented in the model, correctly produce axisymmetric flows.

Plots of thickness and velocity along a radial section are shown in the right panels of Fig. 5 and Fig. 6, for the initial Richardson numbers of 0.1 and 0.9, respectively. These results can be compared with those presented in Engwell et al. (2016), Fig.3, where the same initial parameters have been used. For both initial conditions, model solutions show a decrease in flow thickness immediately after the source which is more pronounced for the largest value of Ri . Then, after approximately 3.5 km

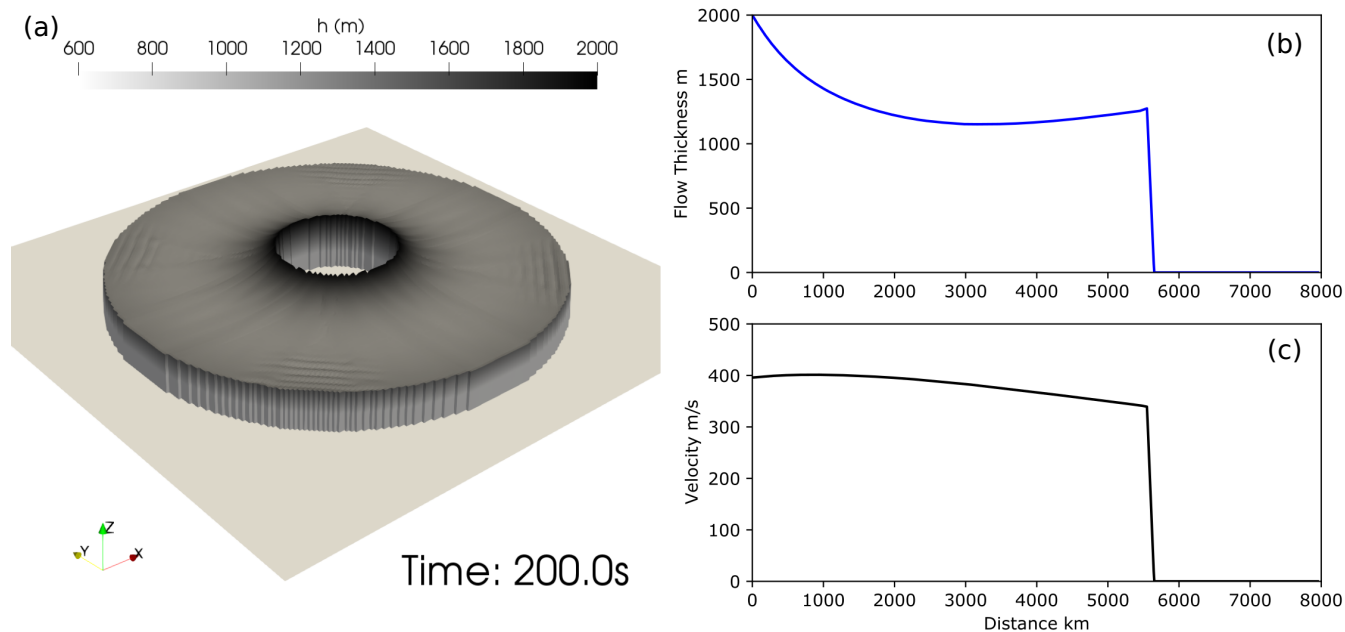


Figure 5. Supercritical flow with initial $Ri=0.1$. The solution is computed only for the cells of the computational domain outside (fully or partially) $R = 2000$ m. The color of the free surface represents flow thickness.

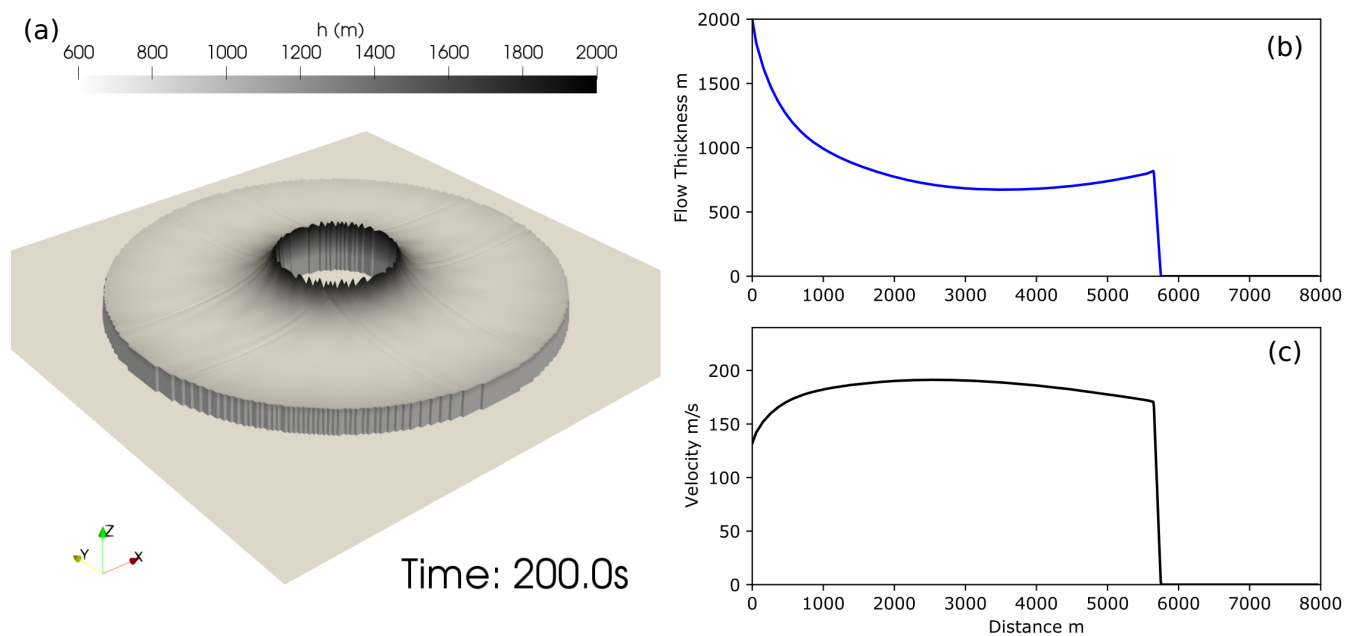


Figure 6. Supercritical flow with initial $Ri=0.9$. The solution is computed only for the cells of the computational domain outside (fully or partially) $R = 2000$ m. The color of the free surface represents flow thickness.

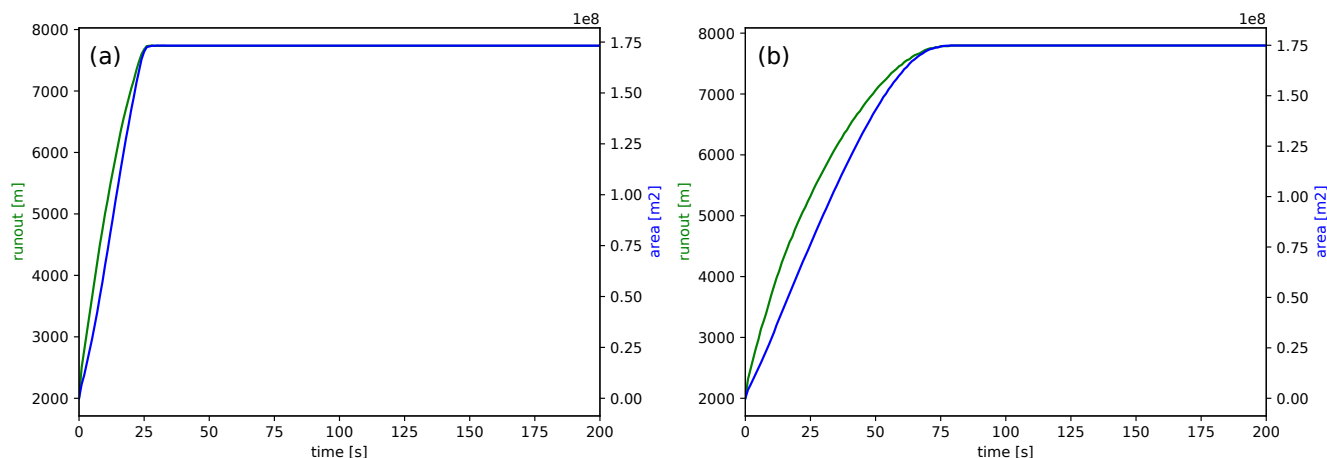


Figure 7. Runout (green line) and area invaded (blue line) versus time for a simulation with initial $Ri = 0.1$ (left panel) and $Ri = 0.9$ (right panel).

470 from the source, thickness increases again. These two different trends are due to the superposition of the thinning associated with the radial spreading and the thickening associated with atmospheric air entrainment, the first being more important close the source and the second at greater distances (see also Calabrò et al., 2022). The velocity profiles of the two simulations present larger differences in the absolute values than the thickness, mostly because of the initial velocities associated with the different Richardson numbers. At the maximum runout distances, which are comparable for the two simulations, this results
475 in a residual momentum for the simulation with $Ri = 0.1$ being almost twice that for the simulation with $Ri = 0.9$, as shown also by (Engwell et al., 2016).

An advantage of a transient model, with respect to a steady one, is that the simulation can provide information on the propagation of the flow and the time needed to reach the maximum runout. Fig. (7) shows the runout (green line) and the area invaded by the flow (blue line) versus time for the two simulations presented above. In both simulations, we observe an almost
480 linear increase in the area invaded with time, up to the time at which the maximum runout is reached. For the simulation with initial $Ri = 0.1$, and thus with a larger flow velocity, the maximum runout is reached at $t = 28$ s, while for the simulation with initial $Ri = 0.9$ it is reached at $t = 79$ s. Furthermore, we remark that only a transient model can simulate the modifications of the topography associated with the deposition of solid particles, because of the intrinsic transient nature of this process.

6 PDCs over water: the 1883 Krakatau eruption

485 Here we present an application of the model to the 1883 Krakatau eruption, which highlights the capability of the model to treat the interaction of the flow with topography, the presence of hydraulic jumps and the vaporization and entrainment of water.



The Krakatau volcanic system is notorious for eruptive behaviour that interacts with the seas of the surrounding Sunda Straits. In 1883, an eruption produced PDCs that propagated more than 40 km across the sea (Carey et al., 1996), impacting populations on the coastlines of Sumatra and Java (Simpkin and Fiske, 1983), and potentially playing a role in the formation of devastating tsunamis that lead to the deaths of > 36000 people (Maeno and Imamura, 2011). Here, we test the flow model on real topography and investigate topographic effects on flow regime and the transition from supercritical to subcritical flow. In addition, we show the effect of ingestion of sea water in the form of water vapour into the flows.

We test the flow over water model formulation using a contemporary (i.e. representing recent topography rather than that in 1883) 30 metres SRTM Void filled DEM (USGS EarthExplorer downloaded July 2021) of the area around the Krakatau volcanic complex and the Sunda Straits (Fig 8). We assume that all cells with an elevation of zero are water. Model inputs were informed using information from the 1883 eruption from the published record and from field analysis of eruption deposits. An initial flow temperature of 773K (500°C) was used based on results from Mandeville et al. (1994). However, the simulations are not aimed at replicating the eruption, but to give insight into the model application and the possible dynamics of these flows. An initial flow radius of 2 km, flow Richardson number of 0.7 and mass flow rate of $10^9 \text{ m}^3 \text{ s}^{-1}$ were used. The initial density is 40 kgm^{-3} . Initial flow thickness and velocities were calculated from these parameters. A particle class of 100 microns was used, and the gamma coefficient ($\gamma_{i_s, wv}$) was set to 0.86. This value was not constrained by observations, but selected from an ensemble of simulations to better highlight some features of the flow (large entrainment of water vapour, hydraulic jumps, transient dynamics). Flow parameters were analysed along a number of transects (Fig 8), which have different topographic profiles relating to the islands around the volcano (Fig 9). A probe location is used to show how flow properties at a given location change with time.

The source condition of the simulated PDC mimics the initial radial spreading generated by a column collapse, the flow then quickly interacts with the nearby Krakatau islands of Sertung, Rakata and Panjang. The flow overtops the proximal islands of Sertung and Panjang, but it is directed around the much taller island of Rakata, with the flow fronts merging downstream on the far side of the island (Fig 8). The flow runout at 360 and 1320 seconds varies along the different transects (Figs 10 and 11), with runout considerably less along transects 5 and 6 than the other transects, related to the more variable topographic elevation along these transects (Fig 9). Flow temperature shows a gradual decrease with distance from source along most transects. The temperature drops to 300 k along transect 5 at 360 seconds and transect 6 at 1320 seconds. This reflects that at these times, there is no flow at these locations, and the temperature is that of the ambient.

In general, the simulated flow develops larger thicknesses at the head (Figs 10, 11), followed by a thinner body. These changes are related to variations in the Ri number, and air entrainment (Figs 10, 11). In comparison to trends seen in Figs 5 and 6, and results shown by Bursik and Woods (1996); Calabrò et al. (2022); Shimizu et al. (2019), the trends do not show an initial decrease in thickness with distance. This is the result of the large volume of water vapour entrained into the flow, as shown in Fig 11F. Numerical model results using smaller values for the $\gamma_{i_s, wv}$ coefficient (Supplementary Figure 1) show a decrease in flow thickness with distance from source. Flow thickness considerably increases upstream of topographic barriers, such as the islands of Sertung (transect 2) and Panjang (transect 1), which are within a couple of kilometres of the source. This increase is the result of the formation of backward propagating hydraulic jumps, marking the transition from supercritical

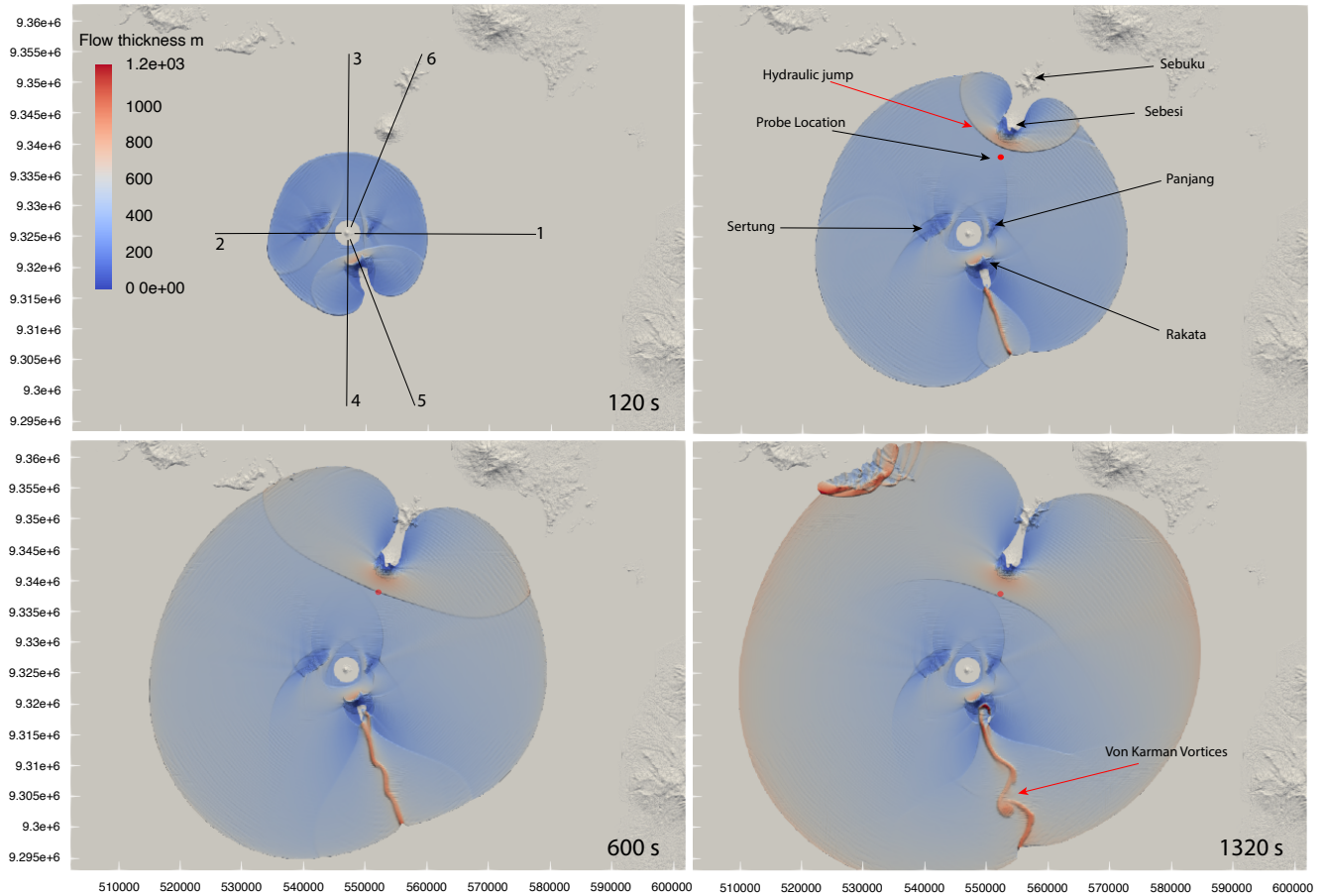


Figure 8. Snapshots of simulation SA4_0003, where a grainsize of 100 microns, a MFR of 10^9 , and a gamma coefficient ($\gamma_{i_s, wv}$) of 0.86 was used. Each image represents a different time step in the simulation. The red marker shows the probe location at 552669E 9338081N UTM. The topographic elevation for each transect is shown in Figure 9.

flows with Richardson numbers less than one to subcritical flow. Downstream of topographic barriers, when the flows are capable of overcoming the obstacle, they transition back from thick, subcritical to thin supercritical flows. The most extreme variation in Richardson numbers occurs along transect 5 at 1320 s, with a high Richardson number upstream of Rakata island, a topographic barrier to the flow, and peaking downstream of the island as the flow converges. This peak in Richardson number is due to a large decrease in velocity, which results in an increased loss of particles and therefore a decrease in solid volume fraction within the flow (Figs 10D).

Downstream of Rakata island (transect 5), the flow thickness at 1320 seconds is highly variable showing multiple peaks and troughs not directly associated with any variation in topography. These thickness variations are the result of the formation of Von Karman vortices that formed in the wake of the topographic high on the island of Rakata, to the SE of the source (Fig 11). Variations in Richardson number for some transects match those shown in 1D simulations presented earlier in the paper

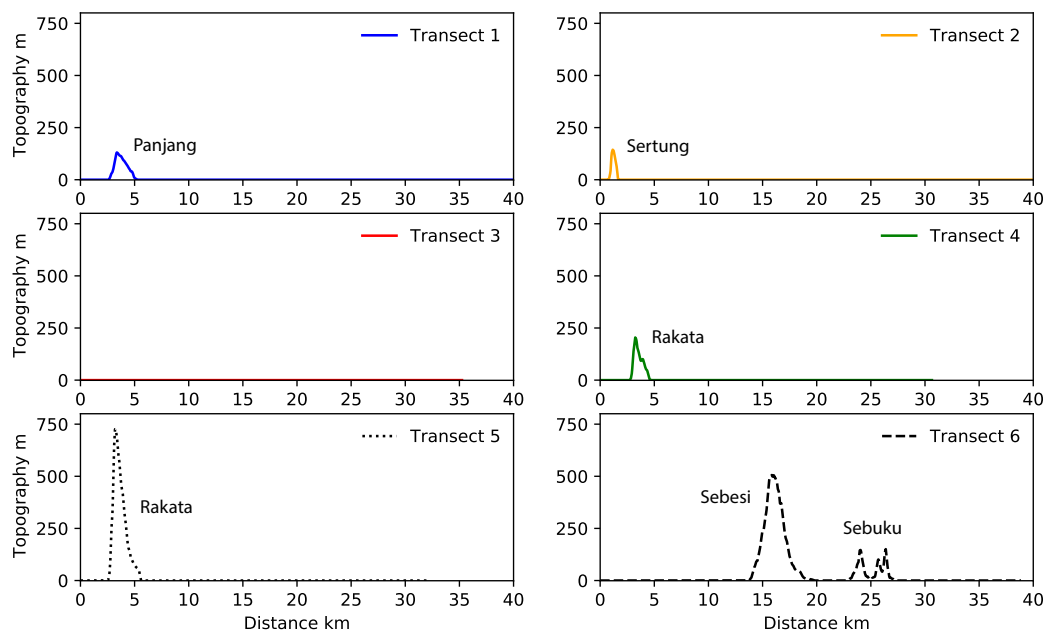


Figure 9. Topographic profiles of transects shown in Figure 8A. Note the vertical exaggeration of the y-axis. Transect 3 is the only transect that does not show variation in elevation along the flow runoff, all other transects cross one of the many islands in the Sunda Strait.

(Fig 4), whereby the transition from super to subcritical flow moves upstream through time. This is shown particularly well for transect 6: at 360 seconds, the transition is clearly visible at a distance of approximately 13 km from source (Fig 11), while at 1320 seconds, it is less well defined and occurs approximately 2 km closer to the source (Fig 11). This transition is also evident
535 when studying the flow interactions with Sebesi Island, to the NE (Fig. 8): the shape of the hydraulic jump front changes from tightly curved around the island at 360 seconds, to a more elongate region at 600 seconds to a concave region bending back towards the Krakatau Islands at 1320 seconds. In Fig 8 the backwards propagation of the hydraulic jump is also evident when
540 looking at the relative position of the transition region with respect to the red marker. This marker represents the probe location at which we sampled flow variables with time to show the effect of the passing hydraulic jump on current characteristics. In
545 Fig 12A we plot dynamic pressure and in Fig 12B, deposit thickness and deposition rate with time. These figures clearly show the arrival of the flow at 130s. The dynamic pressure also shows the passing of the hydraulic jump at approximately 600 s (as also shown in Fig. 8C). The dynamic pressure shows a sharp decrease at approx. 1900 s, 100 s after source emission ends. Flow arrival at the probe location is also shown in Fig 12B, with an increase in flow thickness and deposition rate. After arrival of the flow, the deposition rate is almost constant, resulting in a linear increase in deposit thickness with time, with no change
545 associated with transition from supercritical to subcritical flow. The decay in deposition rate associated with the cessation of the flow is much more gentle than that of dynamic pressure. Variations in flow characteristics also occur along transect 3. At 360 seconds, transect 3 (Fig 10B) shows a sharp increase in thickness at a distance of 16 km from source that at later stages

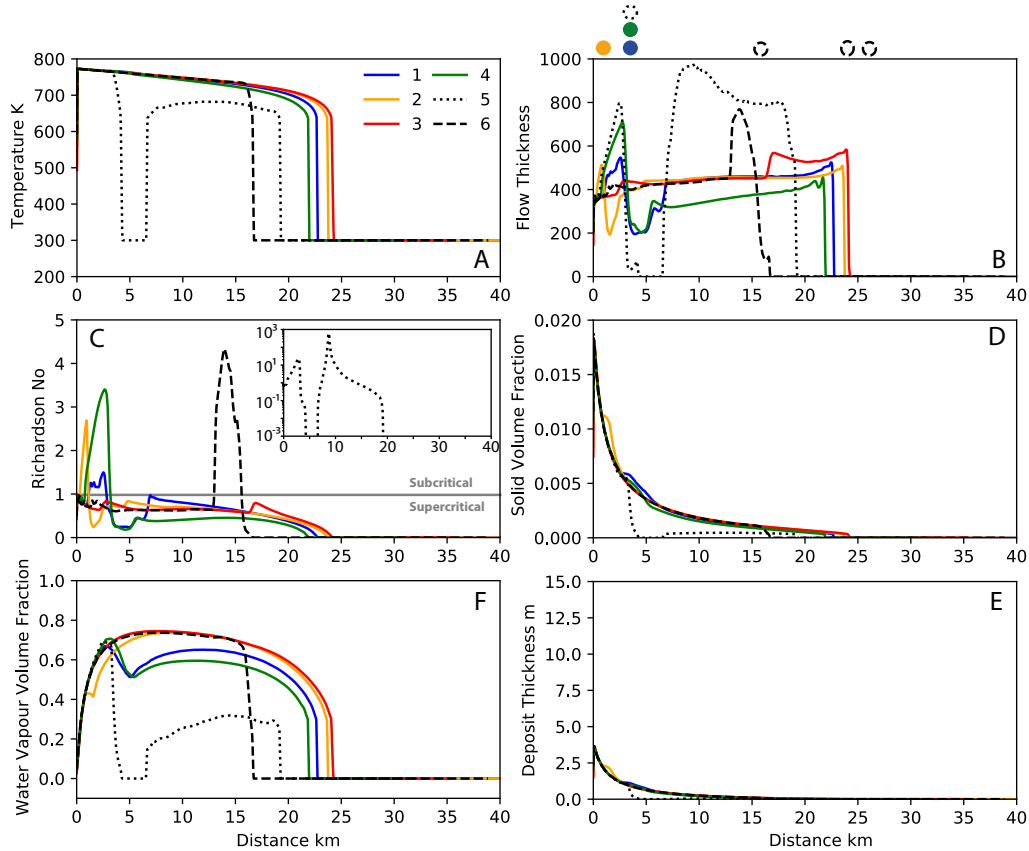


Figure 10. Variation in flow parameters with distance at 360 seconds post flow initiation for simulation SA4_0003, along transects shown in Fig 8. Markers above Panel B show the location of topographic barriers for each transect. The Richardson Number with distance for transect 5 is shown in the inset figure.

develops into a backward propagating hydraulic jump. Fig 9 shows flat topography for this transect, but analysis of Fig 8 shows that the increase in thickness is related to the flow interaction with the island of Sebesi.

550 Trends in deposit thickness closely follow those in solid volume fraction: both decrease exponentially with distance from source (Figs 10 and 11). Solid volume fraction and deposit thickness have slightly lower decay rates at distances of less than 2 km and 5 km for transect 1 and 2 respectively, and more subtly for transect 4 at distances of approximately 5 km. These increases relate to locations where the flow is in a subcritical regime, i.e. the flow is thicker and has higher Richardson numbers, equivalent to lower velocities. These slightly higher values of solid volume fraction, and consequently deposition rates (see Eq. 555 19) are related to flow interaction with topography, whereby the flow slows and thickens, and has higher deposition upstream of barriers. Solid volume fraction and deposit thickness trends differ significantly for transect 5, which has large changes in topographic elevation as it crosses the island of Rakata, close to the source. Both profiles show the same decay as seen in the other transects in the first couple of kilometres from source, before decreasing sharply and, at distances of around 10 km from

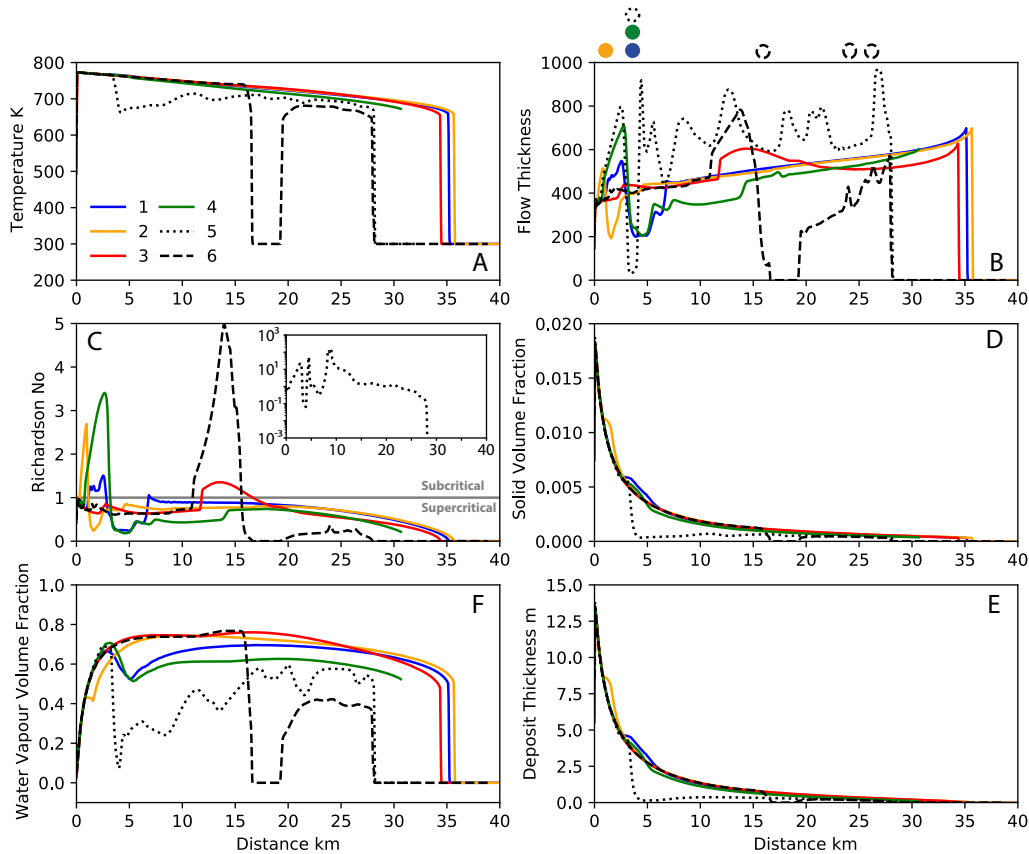


Figure 11. Variation in flow parameters with distance at 1320 seconds post flow initiation for simulation SA4_0003, along transects shown in Fig 8. Markers above Panel B show the location of topographic barriers for each transect. The Richardson Number with distance for transect 5 is shown in the inset figure.

the source, showing a slight increase. These trends can be explained by the flow interaction with Rakata Island, which has a height of > 700 m (Fig 9). The flow is unable to overtop this barrier, and instead flows around it, converging downstream. The decrease to zero solid volume fraction and deposit thickness represents the sheltered part of Rakata island that the flow does not reach (Figs 10 and 11).

Fig 10F and 11F show a general increase and then decrease in water vapour volume fraction of the flow with distance from source. This is shown in greater detail in Fig 13 where water vapour volume fraction is plot alongside the volume fractions of the other flow components. For the $\gamma_{i_s, wv}$ coefficient used in this simulation, we can see that along both transects, the water vapour volume fraction can reach large values up to almost 0.75. The relative amounts of water vapour and atmospheric air also varies as the flows interact with topography, with transect 1 showing a decrease in water vapour and an increase in entrained air as the flow travels over Panjang island to the east. Transect 3 shows steady variations in water vapour and entrained air, with water vapour volume fraction quickly increasing and entrained air decreasing in the first couple of kilometres. There is

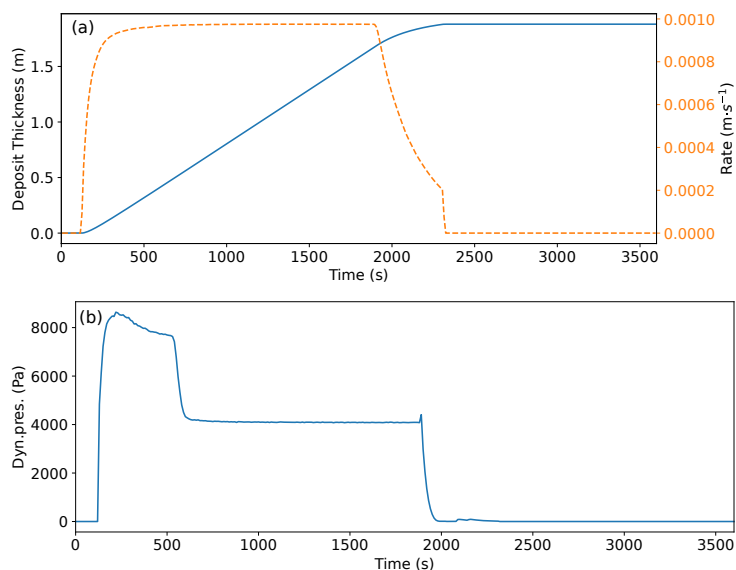


Figure 12. Variation in deposit thickness, rate and dynamic pressure at the probe location shown in Fig 8.

570 then a gradual decrease in the amount of water vapour, and an increase in entrained air over the next 15 km. This is related to a decrease in temperature towards the flow front, which results in lower thermal energy of the depositing particles available for sea water vaporisation. The sharp decrease in water vapour and increase in air corresponds to the flow front. Transect 3 does not intersect any topography, resulting in consistent trends with distance from source at 360 seconds. However, at 1320 seconds, some subtle variation in both water vapour (a slight decrease) and entrained air volume (a slight increase) fraction are
575 seen between 10 and 15 km from source. This is the result of the changing shape of the hydraulic jump that formed around the island of Sebesi. Additional simulations were performed to show the effect of $\gamma_{i_s, wv}$ coefficient of flow characteristics and relevant figures are available in the supplementary materials.

A thorough discussion about the optimal choice of the rheological model and input parameters for PDCs, in particular those over water, requires an extensive comparison with phenomena and events at numerous volcanoes to accurately inform input
580 parameters, and where sufficient observations are available with which to validate model results. More accurate measurements are needed to achieve a better calibration of the model. This, however, is beyond the scope of the present work.

7 Conclusions

We have presented the developments of the physical model and the open source numerical code IMEX_SfloW2D (de' Michieli Vituri et al., 2019). They consist of the generalization of the shallow-water equations to describe a polydisperse fluid-solid mixture, including terms for sedimentation and entrainment of solids and water vapour, transport equations for solid particles of
585 different sizes, transport equations for different components of the carrier phase, and an equation for temperature/energy. Con-

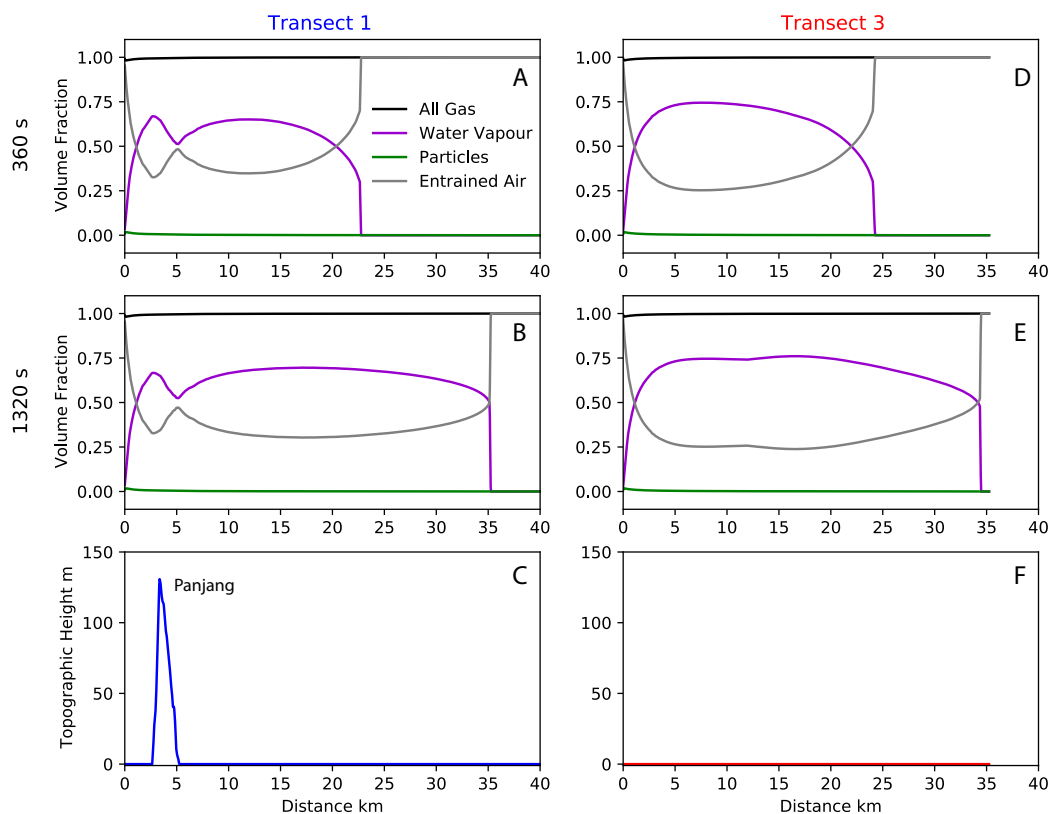


Figure 13. Variation in volume fraction of flow components along transects 1 and 3 at 360 and 1320 seconds post flow initiation.

stitutive equations allow us to adapt the numerical code to solve different types of geophysical mass flows (landslides, debris flows, lahars, snow and rock avalanches, pyroclastic avalanches) and here we have presented its application to the simulation of transient PDCs. The model resolves the depth-averaged flow velocity and density, and does not account for the effects of internal flow stratification. In particular, it cannot be applied to PDCs in which the basal, concentrated flow interacts with the overlaying dilute ash cloud in a two-layer system (Shimizu et al., 2019). It is therefore suited to describe PDCs end-members (either a concentrated pyroclastic avalanche or an inertial PDC). The numerical code has been tested to verify its capability to describe both sub- and supercritical regimes, as appropriate for large-scale, ignimbrite forming eruptions. The results of synthetic numerical benchmarks demonstrate the robustness of the numerical code facing trans-critical flows. Moreover, they highlight the importance of simulating transient in comparison to steady-state flows, and flows in 2D versus 1D currents. Finally, the example application to the Krakatau 1883 eruption, shows the capability of the numerical model to face a complex natural case involving the propagation of PDCs over the sea surface and across topographic obstacles, showing the relevance, at the large scale, of non-linear fluid dynamic features, such as hydraulic jumps and Van Karman vortices.



Code availability. The numerical code, benchmark tests and documentation are available at https://github.com/demichie/IMEX_SfloW2D_v2 (last access: 16 December 2022). Preprocessing scripts (to change the grid resolution and the numerical schemes) and post-processing scripts (to plot the solution variables and to create animations) are also available. Furthermore, some of the examples presented in this paper have a page description on the model Wiki (https://github.com/demichie/IMEX_SfloW2D_v2/wiki, last access: 16 December 2022), where detailed information on how to run the simulations is given. The digital object identifier (DOI) for the version of the code documented in this paper is <https://doi.org/10.5281/zenodo.7476737>.

605 Appendix A: Derivation of depth-averaged governing equations for variable density flows

In this appendix we present the derivation of the depth-averaged momentum and energy equations. For the sake of simplicity, we present the derivation by considering the ordinary gravity g , instead of the reduced gravity g' , and without friction terms. Furthermore, we present the derivation for a flow over a 1D topography parallel to the x axis. In this case, $B = B(x, t)$ and $h = h(x, t)$ are function of x and t only, and the velocity vector is $\mathbf{v} = (u, w)$, where u and w are the horizontal and vertical components, respectively (see Fig. A1).

A1 Momentum equation

The momentum equation is derived by integrating the Navier-Stokes equations in conservative form over the thickness of the flow, and by applying appropriate boundary conditions at the top (free surface) and the bottom (topography) of the flow.

For a flow with no mass exchange with the surrounding environment and over an impermeable terrain constant in time ($\frac{\partial B}{\partial t} = 0$), the following kinematic conditions at the free surface and at the flow bottom (Johnson, 1997) are usually employed:

$$\frac{\partial(B+h)}{\partial t} = w(x, B+h, t) - u(x, B+h, t) \frac{\partial(B+h)}{\partial x}$$
$$w(x, B, t) - u(x, B, t) \frac{\partial B}{\partial x} = 0.$$

The first condition states that the (moving) free-surface must be always composed of fluid particles, i.e. that the free-surface elevation changes at a rate equal to the velocity of the flow in the direction perpendicular to the surface. The second condition states that the fluid velocity directed perpendicular to a solid boundary must vanish on the boundary itself.

However, here we consider atmospheric air entrainment and solid sedimentation, which affect both the topography and the free-surface elevations. For this reason, the classical equations presented above are modified in the following way:

$$\frac{\partial B}{\partial t} + u(x, B, t) \frac{\partial B}{\partial x} - w(x, B, t) = \sum_{i_s=1}^{n_s} D_{s, i_s},$$

$$\frac{\partial(B+h)}{\partial t} + u(x, B+h, t) \frac{\partial(B+h)}{\partial x} - w(x, B+h, t) = E_a.$$

In a 2D static Eulerian frame of reference (see Fig. A1), the momentum equation for horizontal component of the velocity for a generic fluid parcel at the point (x, z) and with velocity (u, w) , without shear stress and external forces, writes in the

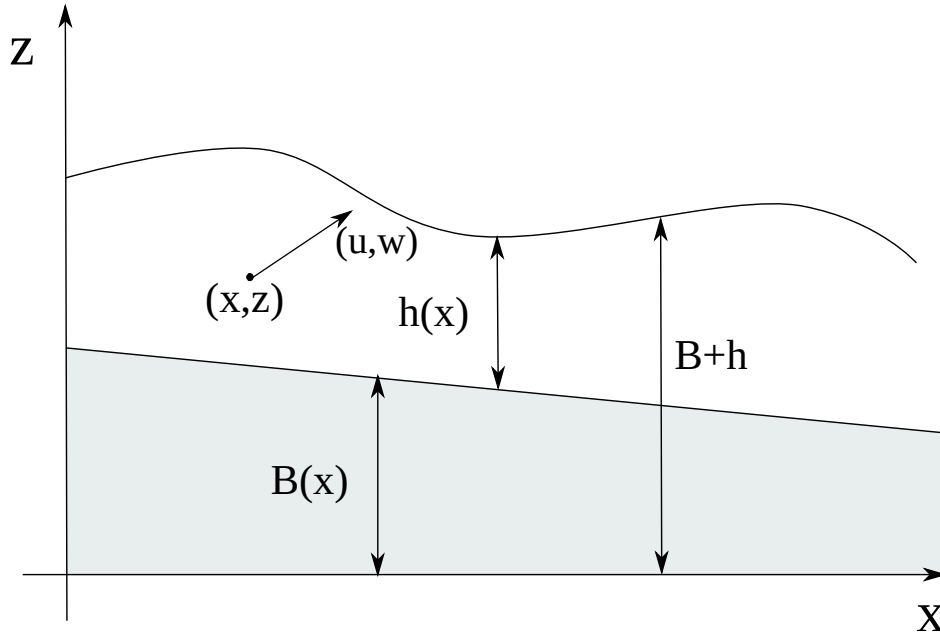


Figure A1. Model variables for a 1D flow. B is the topography elevation, h denotes flow thickness and u and w are the horizontal and vertical components at the point (x, z) .

following way (Anderson and Wendt, 1995, Eq. 2.42a):

$$\frac{\partial(\rho_m u)}{\partial t} + \frac{\partial(\rho_m u^2)}{\partial x} + \frac{\partial(\rho_m u w)}{\partial y} = -\frac{\partial p}{\partial x}. \quad (\text{A.1})$$

If we integrate between B and $B + h$ on both sides of the equation, we can apply the Leibniz rule to the first term of the
 630 vertically integrated momentum conservation equation, obtaining:

$$\int_B^{B+h} \frac{\partial(\rho_m u)}{\partial t} dz = \frac{\partial}{\partial t} \int_B^{B+h} \rho_m u dz + \rho_m u(B) \frac{\partial B}{\partial t} - \rho_m u(B+h) \frac{\partial(B+h)}{\partial t} =$$

$$\frac{\partial}{\partial t} (\rho_m h \bar{u}) + \rho_m u(B) \frac{\partial B}{\partial t} - \rho_m u(B+h) \frac{\partial(B+h)}{\partial t},$$

where in the last equality we assumed that the density does not vary with depth, and where we denoted with \bar{u} the depth-averaged horizontal velocity:

$$635 \quad \bar{u} = \frac{1}{h} \int_B^{B+h} u dz.$$



In a similar way, we apply the Leibniz rule to the integral of the second term on the left-hand side of the momentum equation:

$$\int_B^{B+h} \frac{\partial(\rho_m u^2)}{\partial x} dz = \frac{\partial}{\partial x} \int_B^{B+h} \rho_m u^2 dz + \rho_m u^2(B) \frac{\partial B}{\partial x} - \rho_m u^2(B+h) \frac{\partial(B+h)}{\partial x} =$$

$$\frac{\partial(\rho_m h \bar{u}^2)}{\partial x} + \rho_m u^2(B) \frac{\partial B}{\partial x} - \rho_m u^2(B+h) \frac{\partial(B+h)}{\partial x}$$

where we denoted with \bar{u}^2 the depth-averaged value of the square of the horizontal velocity:

$$640 \quad \bar{u}^2 = \frac{1}{h} \int_B^{B+h} u^2 dz.$$

For the integral of the last term on the left-hand side of the momentum equation we can apply the fundamental theorem of calculus:

$$\int_B^{B+h} \frac{\partial \rho_m u w}{\partial z} dz = \rho_m u(B+h) w(B+h) - \rho_m u(B) w(B).$$

Thus, by summing the three terms, the integral of the left-hand side of the momentum equation A.1 is:

$$\frac{\partial}{\partial t} (\rho_m h \bar{u}) + \frac{\partial}{\partial x} (\rho_m h \bar{u}^2) + \rho_m \tilde{u}(B) \left[\frac{\partial B}{\partial t} + u(B) \frac{\partial B}{\partial x} - w(B) \right]$$

$$- \rho_m \tilde{u}(B+h) \left[\frac{\partial(B+h)}{\partial t} + w(B+h) - u(B+h) \frac{\partial(B+h)}{\partial x} \right].$$

In the previous equation, we denoted with the symbol \tilde{u} the horizontal velocities at the bottom and at the free surface
 645 interfaces. It is important to observe that at each of these interfaces we have two different velocities, one internal to the fluid
 and one external, and \tilde{u} represents the velocity that contribute to the change in the terrain elevation or in the free-surface
 elevation. The first one changes because of particle sedimentation from the flow, so the velocity to consider is that of the flow.
 Conversely, the free-surface elevation change is associated with entrainment of atmospheric air, which we assume still. For
 this reason, $\tilde{u}(B+h) = 0$, and the last term is neglected, resulting in a simpler form of the integral of the left-hand side of the
 650 momentum equation:

$$\frac{\partial}{\partial t} (\rho_m h \bar{u}) + \frac{\partial}{\partial x} (\rho_m h \bar{u}^2) + \rho_m u(B) \sum_{i_s=1}^{n_s} D_{s,i_s}$$

For the integral of the right-hand side of the momentum equation (pressure term), we assume an hydrostatic pressure profile,
 i.e.:

$$p(x, z, t) = \int_z^{B+h} \frac{\partial p(x, z, t)}{\partial z} dz = \rho g (B+h-z) \tag{A.2}$$

655 To integrate the pressure term, we apply again the Leibniz rule to compute the term



$$\int_B^{B+h} \frac{\partial p(x, z, t)}{\partial x} dz = \frac{\partial}{\partial x} \int_B^{B+h} p(x, z, t) dz + p(x, B, t) \frac{\partial B}{\partial x}$$

$$-p(x, B+h, t) \frac{\partial}{\partial x} (B+h) = \frac{\partial}{\partial x} \left[-\rho_m g \frac{(B+h-z)^2}{2} \right]_B^{B+h} + \rho_m g h \frac{\partial B}{\partial x}$$

$$= -\frac{\partial}{\partial x} \left[\rho_m g \frac{h^2}{2} \right] + \rho_m g h \frac{\partial B}{\partial x}$$

If we assume that the vertical variations of the horizontal velocity are negligible, we can replace \bar{u} and \bar{u}^2 with u and u^2 , respectively, where u represents the depth-averaged horizontal component of the velocity. With this assumption, combining the expression obtained for the integral of the left- and right-hand side of the momentum equation, we obtain the following equation:

$$\frac{\partial}{\partial t} (\rho_m h u) + \frac{\partial}{\partial x} (\rho_m h u^2) = -\rho_m u \sum_{i_s=1}^{n_s} D_{s,i_s} + \frac{\partial}{\partial x} \left[\rho_m g \frac{h^2}{2} \right] - \rho_m g h \frac{\partial B}{\partial x}. \quad (\text{A.3})$$

In Eq. (A.2), for the sake of simplicity, we neglected the contribution of the atmospheric pressure in the hydrostatic pressure, by assuming that the pressure is null at the free-surface. When the contribution of the atmospheric pressure is considered, we obtain an equation with the reduced gravity instead of the ordinary gravity.

A2 Derivation of energy equation for variable density flows

In this appendix we present the derivation of the the depth-averaged total energy equation, under the same assumption that led to the derivation of the depth-averaged momentum equation.

The desired equation is obtained by integrating over the flow depth the total energy equation for a 2D flow without shear stress (Anderson and Wendt, 1995, Eq. 2.64):

$$\frac{\partial}{\partial t} \left[\rho_m \left(e + \frac{u^2 + w^2}{2} \right) \right] + \frac{\partial}{\partial x} \left[\rho_m \left(e + \frac{u^2 + w^2}{2} \right) u \right]$$

$$+ \frac{\partial}{\partial z} \left[\rho_m \left(e + \frac{u^2 + w^2}{2} \right) w \right] = -\frac{\partial (up)}{\partial x} - \frac{\partial (wp)}{\partial z} + w \rho_m g.$$

where $e = C_v T$ is the internal energy of the flow.

By using the Leibniz rule, the integral of the first term of the left-hand side of the energy equation is:

$$\int_B^{B+h} \frac{\partial}{\partial t} \left[\rho_m \left(e + \frac{u^2 + w^2}{2} \right) \right] dz = \frac{\partial}{\partial t} \int_B^{B+h} \left[\rho_m \left(e + \frac{u^2 + w^2}{2} \right) \right] dz$$

$$+ \left[\rho_m \left(e + \frac{u^2 + w^2}{2} \right) \right]_{z=B} \frac{\partial B}{\partial t} - \left[\rho_m \left(e + \frac{u^2 + w^2}{2} \right) \right]_{z=B+h} \frac{\partial (B+h)}{\partial t}$$



Proceeding in a similar way, the second term can be written as:

$$680 \int_B^{B+h} \frac{\partial}{\partial x} \left[\rho_m \left(e + \frac{u^2 + w^2}{2} \right) u \right] dz = \frac{\partial}{\partial x} \int_B^{B+h} \left[\rho_m \left(e + \frac{u^2 + w^2}{2} \right) u \right] dz$$

$$\left[\rho_m \left(e + \frac{u^2 + w^2}{2} \right) u \right]_{z=B} \frac{\partial B}{\partial x} - \left[\rho_m \left(e + \frac{u^2 + w^2}{2} \right) u \right]_{z=B+h} \frac{\partial(B+h)}{\partial x}$$

For the integration of the third term of the left-hand side, we apply the fundamental theorem of calculus:

$$\int_B^{B+h} \frac{\partial}{\partial z} \left[\rho_m \left(e + \frac{u^2 + w^2}{2} \right) w \right] dz =$$

$$\left[\rho_m \left(e + \frac{u^2 + w^2}{2} \right) w \right]_{z=B+h} - \left[\rho_m \left(e + \frac{u^2 + w^2}{2} \right) w \right]_{z=B}$$

685 If we assume that T and ρ_m and u do not vary with depth, then we can write the left-hand side of the energy equation in the following way

$$\frac{\partial}{\partial t} \left[\rho_m h \left(e + \frac{\overline{u^2} + \overline{w^2}}{2} \right) \right] + \frac{\partial}{\partial x} \left[\rho_m h \left(e \bar{u} + \frac{\overline{u^3} + u \overline{w^2}}{2} \right) \right]$$

$$- \left[\rho_m \left(e + \frac{u^2 + w^2}{2} \right) \right]_{z=B+h} \left[\frac{\partial(B+h)}{\partial t} + u(B+h) \frac{\partial(B+h)}{\partial x} - w(B+h) \right]$$

$$+ \left[\rho_m \left(e + \frac{u^2 + w^2}{2} \right) \right]_{z=B} \left[\frac{\partial B}{\partial t} + u(B) \frac{\partial B}{\partial x} - w(B) \right]$$

690 As for the momentum equation, we observe that the terms in the square brackets depending on the free-surface and topography elevation are associated with air entrainment and particle sedimentation rates. Furthermore, it is important to remark that air entrainment does not carry any kinetic energy in the flow, but only thermal energy, while both energies are lost due to particle sedimentation. With this in mind, we can rewrite the equation above in the following way:

$$\frac{\partial}{\partial t} \left[\rho_m h \left(e + \frac{\overline{u^2} + \overline{w^2}}{2} \right) \right] + \frac{\partial}{\partial x} \left[\rho_m h \left(e \bar{u} + \frac{\overline{u^3} + u \overline{w^2}}{2} \right) \right]$$

$$- \rho_a C_a T_a E_a + \sum_{i_s=1}^{n_s} \left[\rho_{s,i_s} \left(C_{s,i_s} T + \frac{u(B)^2 + w(B)^2}{2} \right) \right] D_{s,i_s}$$



695 We compute now the integral of the pressure and gravitational terms. The first term on the right-hand side of the energy equation can be integrated by applying the Leibniz rule:

$$\int_B^{B+h} \frac{\partial(wp)}{\partial x} dz = \frac{\partial}{\partial x} \int_B^{B+h} p(x, z, t) u(x, z, t) dz$$

$$+ p(x, B, t) u(x, B, t) \frac{\partial B}{\partial x} - p(x, B+h, t) u(x, B+h, t) \frac{\partial(B+h)}{\partial x} =$$

$$\frac{\partial}{\partial x} \int_B^{B+h} p(x, z, t) u(x, z, t) dz + \rho_m g h u(B) \frac{\partial B}{\partial x}$$

700

. In the second equality, the last term on the left-hand side is null because we assumed the hydrostatic pressure is null at the free surface. In the equation above, the integral of the product of the pressure and the horizontal velocity is computed by approximating the horizontal velocity with \bar{u} and by substituting $p(z) = \rho_m g(B+h-z)$, obtaining

$$\frac{\partial}{\partial x} \int_B^{B+h} p(x, z, t) \bar{u}(x, t) dz =$$

$$\frac{\partial}{\partial x} \left[u(x, t) \int_B^{B+h} \rho_m g(B+h-z) dz \right] = \frac{\partial}{\partial x} \left[\rho_m g \bar{u} \frac{h^2}{2} \right]$$

705

The second pressure term on the right-hand side of the energy equation, when integrated over the flow depth, is:

$$\int_B^{B+h} \frac{\partial(wp)}{\partial z} dz = p(x, B+h, t) w(x, B+h, t) - p(x, B, t) w(x, B, t) = -\rho_m g h w(B+h)$$

This term, if we assume that the variations of the vertical component of the velocity with flow depth are negligible, cancels out with the integral of the work done by the gravitational force:

$$\int_B^{B+h} w \rho_m g = \rho_m g h \bar{w}$$

710

Now, if we sum all the terms, we have:

$$\frac{\partial}{\partial t} \left[\rho_m h \left(e + \frac{\bar{u}^2 + \bar{w}^2}{2} \right) \right] + \frac{\partial}{\partial x} \left[\rho_m h \left(e \bar{u} + \frac{\bar{u}^3 + \bar{u} \bar{w}^2}{2} \right) \right]$$

$$+ \frac{\partial}{\partial x} \left[\rho_m g \bar{u} \frac{h^2}{2} \right] = -\rho_m g h u(B) \frac{\partial B}{\partial x}$$

$$- \rho_a C_a T_a E_a + \sum_{i_s=1}^{n_s} \left[\rho_{s, i_s} \left(C_{s, i_s} T + \frac{u(B)^2 + w(B)^2}{2} \right) \right] D_{s, i_s}$$

715 If we neglect the contribution of the vertical component of the velocity to the kinetic energy, and we assume that the horizontal velocity is constant ($u(z) = \bar{u}$), we have:



$$\frac{\partial}{\partial t} \left[\rho_m h \left(e + \frac{u^2}{2} \right) \right] + \frac{\partial}{\partial x} \left[\rho_m h u \left(e + \frac{u^2}{2} \right) + \rho_m g u \frac{h^2}{2} \right] = -\rho_m g h u \frac{\partial B}{\partial x} + \rho_a C_a T_a E_a - \sum_{i_s=1}^{n_s} \left[\rho_{s,i_s} \left(C_{s,i_s} T + \frac{u(B)^2 + w(B)^2}{2} \right) \right] D_{s,i_s}.$$

By neglecting the vertical component of the velocity we have a small error in the kinetic energy. For this reason, when the equation for the total energy is solved, and the temperature is computed from the total energy, a small error is also present in the temperature.

A3 Derivation of primitive variables from conservative variables

The model solves for the following set of conservative variables:

$$\mathbf{Q} = (Q_1, \dots, Q_{5+n_s}) = (\rho_m h, \rho_m h u, \rho_m h v, \rho_m e h, h \rho_{s_1} \alpha_{s_1}, \dots, h \rho_{s_n} \alpha_{s_n}, h \rho_{wv} \alpha_{wv}). \quad (\text{A.4})$$

In order to evaluate the fluxes and the other terms in the governing equations, we need to write, in terms of (Q_1, \dots, Q_{4+n_s}) , the primitive variable $\mathbf{P} = (h, hu, hv, T, \alpha_{s_1}, \dots, \alpha_{n_s}, u, v)$, which completely define the state. In this appendix we describe the procedure implemented in the code to compute these quantities from the conservative variables.

First of all, mass fractions of solid phases and water vapour are computed as:

$$x_{s,i_s} = \frac{Q_{4+i_s}}{Q_1} \quad i_s = 1, \dots, n_s \quad x_{wv} = \frac{Q_{5+n_s}}{Q_1} \quad (\text{A.5})$$

and these allow also to obtain mass fraction of air:

$$x_a = 1 - \sum_{i_s=1}^{n_s} x_{s,i_s} - x_{wv} \quad (\text{A.6})$$

In this way, mass averaged quantities of the averaged specific heat C_v can be written in the following way:

$$C_{mix} = \sum_{i_s=1}^{n_s} x_{s,i_s} C_{s,i_s} + x_{wv} C_{wv} + x_a C_a \quad (\text{A.7})$$

Once the average specific heat is known, temperature can be computed from the total specific energy, expressed by Q_4 , in the following way:

$$h \rho_m C_v T = \left[Q_4 - \frac{Q_2^2 + Q_3^2}{2Q_1} \right] \Rightarrow T = \frac{1}{Q_1 C_v} \left[Q_4 - \frac{Q_2^2 + Q_3^2}{2Q_1} \right] \quad (\text{A.8})$$

From the temperature it is possible, through the equation of state, to calculate the density of air ($\rho_a = \frac{P}{R_a T}$) and water vapour ($\rho_{wv} = \frac{P}{R_{wv} T}$), and then the density of the mixture:

$$\frac{1}{\rho_{mix}} = \sum_{i_s=1}^{n_s} \frac{x_{s,i_s}}{\rho_{s,i_s}} + \frac{x_a}{\rho_a} + \frac{x_{wv}}{\rho_{wv}} \quad (\text{A.9})$$



740 Mixture density is used to compute flow thickness and volume fractions:

$$h = \frac{Q_1}{\rho_{mix}}, \quad \alpha_{s,i_s} = \frac{x_{s,i_s} \rho_{mix}}{\rho_{s,i_s}}, \quad \alpha_{wv} = \frac{x_{wv} \rho_{mix}}{\rho_{wv}}, \quad \alpha_a = \frac{x_a \rho_{mix}}{\rho_a} \quad (\text{A.10})$$

Flow velocities are computed from the conservative variables. Here, as done in ..., a desingularization is applied, in order to avoid division by very small numbers and thus velocities too large.

$$u = \frac{\sqrt{2} Q_1 Q_2}{\sqrt{Q_1^4 + \max(Q_1^4, \epsilon)}}, \quad v = \frac{\sqrt{2} Q_1 Q_3}{\sqrt{Q_1^4 + \max(Q_1^4, \epsilon)}}. \quad (\text{A.11})$$

745 Finally, volumetric fluxes hu and hv are not computed directly from the conservative variables, but from the primitive variables obtained from Eqs. (A.10) and (A.11):

$$hu = h \cdot u, \quad hv = h \cdot v. \quad (\text{A.12})$$

Author contributions. MdMV has developed the numerical algorithm, implemented the Fortran code and designed the 1D numerical tests. MdMV, TEO and SE contributed to the model formulation and application in the context of volcanological applications. MdMV and SE
750 wrote the manuscript and produced the figures with contributions from TEO.

Competing interests. The contact author has declared that none of the authors has any competing interests.

Acknowledgements. MdMV and TEO were supported by the INGV project Pianeta Dinamico (CUP D53J19000170001) funded by MIUR (“Fondo finalizzato al rilancio degli investimenti delle amministrazioni centrali dello Stato e allo sviluppo del Paese,” legge 145/2018), Tema
755 8-PANACEA. SLE was supported by a Horizon2020 Eurovolc Transnational Access Grant and funding from NERC Grants NE/T002026/1 and NE/S003509/1.



References

- Anderson, J. D. and Wendt, J.: Computational fluid dynamics, vol. 206, Springer, 1995.
- 760 Bartelt, P., Salm, L. B., and Gruberl, U.: Calculating dense-snow avalanche runout using a Voellmyfluid model with active/passive longitudinal straining, *Journal of Glaciology*, 45, 242–254, <https://doi.org/10.3189/002214399793377301>, 1999.
- Biagioli, E., Vitturi, M. d. M., and Di Benedetto, F.: Modified shallow water model for viscous fluids and positivity preserving numerical approximation, *Applied Mathematical Modelling*, 94, 482–505, 2021.
- Bouchut, F. and Westdickenberg, M.: Gravity driven shallow water models for arbitrary topography, *Communications in Mathematical Sciences*, 2, 359–389, 2004.
- 765 Branney, M. J. and Kokelaar, P.: Pyroclastic density currents and the sedimentation of ignimbrites, Geological Society of London, 2002.
- Bürger, R. and Wendland, W. L.: Sedimentation and suspension flows: Historical perspective and some recent developments, *Journal of Engineering Mathematics*, 41, 101–116, 2001.
- Bursik, M. I. and Woods, A. W.: The dynamics and thermodynamics of large ash flows, *Bulletin of Volcanology*, 58, 175–193, <https://doi.org/10.1007/s004450050134>, 1996.
- 770 Calabrò, L., Esposti Ongaro, T., Giordano, G., and de' Michieli Vitturi, M.: Reconstructing Pyroclastic Currents' Source and Flow Parameters from Deposit Characteristics and Numerical Modelling: The Pozzolane Rosse Ignimbrite case study (Colli Albani, Italy), *Journal of Geophysical Research: Solid Earth*, p. e2021JB023637, 2022.
- Capra, L., Norini, G., Groppelli, G., Macías, J. L., and Arce, J. L.: Volcanic hazard zonation of the Nevado de Toluca volcano, México, *Journal of Volcanology and Geothermal Research*, 176, 469–484, 2008.
- 775 Carey, S., Sigurdsson, H., Mandeville, C., and Bronto, S.: Pyroclastic flows and surges over water: an example from the 1883 Krakatau eruption, *Bulletin of Volcanology*, 57, <https://doi.org/10.1007/BF00304435>, 1996.
- Chow, V.: Open-channel hydraulics, 1959.
- Christen, M., Kowalski, J., and Bartelt, P.: RAMMS: Numerical simulation of dense snow avalanches in three-dimensional terrain, *Cold Regions Science and Technology*, 63, 1–14, 2010.
- 780 Costa, A. and Macedonio, G.: Numerical simulation of lava flows based on depth-averaged equations, *Geophysical Research Letters*, 32, 2005.
- de' Michieli Vitturi, M. and Pardini, F.: PLUME-MoM-TSM 1.0. 0: a volcanic column and umbrella cloud spreading model, *Geoscientific Model Development*, 14, 1345–1377, 2021.
- de' Michieli Vitturi, M., Esposti Ongaro, T., Lari, G., and Aravena, A.: IMEX_SfloW2D 1.0: a depth-averaged numerical flow model for
785 pyroclastic avalanches, *Geoscientific Model Development*, 12, 581–595, 2019.
- Delestre, O., Lucas, C., Ksinant, P.-A., Darboux, F., Laguerre, C., Vo, T.-N.-T., James, F., and Cordier, S.: SWASHES: a compilation of shallow water analytic solutions for hydraulic and environmental studies, *International Journal for Numerical Methods in Fluids*, 72, 269–300, 2013.
- Denlinger, R. P. and Iverson, R. M.: Flow of variably fluidized granular masses across three-dimensional terrain: 2. Numerical predictions
790 and experimental tests, *Journal of Geophysical Research*, 106, 553, <https://doi.org/10.1029/2000jb900330>, 2001.
- Diaz, M. J. C., Kurganov, A., and de Luna, T. M.: Path-conservative central-upwind schemes for nonconservative hyperbolic systems, *ESAIM: Mathematical Modelling and Numerical Analysis*, 53, 959–985, 2019.



- Dufek, J.: The Fluid Mechanics of Pyroclastic Density Currents, *Annual Review of Fluid Mechanics*, 48, annurev-fluid-122414-034252-27, 2015.
- 795 Dufek, J., Manga, M., and Staedter, M.: Littoral blasts: Pumice-water heat transfer and the conditions for steam explosions when pyroclastic flows enter the ocean, *Journal of Geophysical Research: Solid Earth*, 112, 2007.
- Dufek, J., Ongaro, T. E., and Roche, O.: Pyroclastic density currents: processes and models, in: *The encyclopedia of volcanoes*, pp. 617–629, Elsevier, 2015.
- Engwell, S., de' Michieli Vitturi, M., Esposti Ongaro, T., and Neri, A.: Insights into the formation and dynamics of coignimbrite plumes
800 from one-dimensional models, *Journal of Geophysical Research: Solid Earth*, 121, 4211–4231, 2016.
- Fagents, S. A. and Baloga, S. M.: Toward a model for the bulking and debulking of lahars, *Journal of Geophysical Research: Solid Earth*, 111, 2006.
- Fernández-Nieto, E. D., Bouchut, F., Bresch, D., Diaz, M. C., and Mangeney, A.: A new Savage–Hutter type model for submarine avalanches and generated tsunamis, *Journal of Computational Physics*, 227, 7720–7754, 2008.
- 805 Fjordholm, U. S., Mishra, S., and Tadmor, E.: Well-balanced and energy stable schemes for the shallow water equations with discontinuous topography, *Journal of Computational Physics*, 230, 5587–5609, 2011.
- Fyhn, E. H., Lervåg, K. Y., Ervik, Å., and Wilhelmsen, Ø.: A consistent reduction of the two-layer shallow-water equations to an accurate one-layer spreading model, *Physics of Fluids*, 31, 122103, 2019.
- Goutal, N.: Proceedings of the 2nd workshop on dam-break wave simulation, Department Laboratoire National d'Hydraulique, Groupe
810 Hydraulique Fluviale, 1997.
- Houghton, D. D. and Kasahara, A.: Nonlinear shallow fluid flow over an isolated ridge, *Communications on Pure and Applied Mathematics*, 21, 1–23, 1968.
- Hyman, D. M., Dietterich, H. R., and Patrick, M. R.: Toward Next-Generation Lava Flow Forecasting: Development of a Fast, Physics-Based Lava Propagation Model, *Journal of Geophysical Research: Solid Earth*, 127, e2022JB024998, 2022.
- 815 Iga, S.-i. and Matsuda, Y.: Shear instability in a shallow water model with implications for the Venus atmosphere, *Journal of the atmospheric sciences*, 62, 2514–2527, 2005.
- Iverson, R. M. and Denlinger, R. P.: Flow of variably fluidized granular masses across three-dimensional terrain: 1. Coulomb mixture theory, *Journal of Geophysical Research: Solid Earth*, 106, 537–552, <https://doi.org/10.1029/2000jb900329>, 2001.
- Johnson, C. G., Hogg, A. J., Huppert, H. E., Sparks, R. S. J., Phillips, J. C., Slim, A. C., and Woodhouse, M. J.: Modelling intrusions through
820 quiescent and moving ambients, *Journal of Fluid Mechanics*, 771, 370–406, 2015.
- Johnson, R. S.: *A modern introduction to the mathematical theory of water waves*, 19, Cambridge university press, 1997.
- Kelfoun, K. and Druitt, T. H.: Numerical modeling of the emplacement of Socompa rock avalanche, Chile, *Journal of Geophysical Research: Solid Earth* (1978–2012), 110, <https://doi.org/10.1029/2005JB003758>, 2005.
- Kelfoun, K., Samaniego, P., Palacios, P., and Barba, D.: Testing the suitability of frictional behaviour for pyroclastic flow simulation by
825 comparison with a well-constrained eruption at Tungurahua volcano (Ecuador), *Bulletin of volcanology*, 71, 1057–1075, 2009.
- Khezri, N.: Modelling turbulent mixing and sediment process beneath tidal bores: physical and numerical investigations, Ph.D. thesis, School of Civil Engineering, The University of Queensland, 2014.
- Kurganov, A. and Petrova, G.: A second-order well-balanced positivity preserving central-upwind scheme for the Saint-Venant system, *Communications in Mathematical Sciences*, 5, 133–160, 2007.



- 830 Kurganov, A., Noelle, S., and Petrova, G.: Semidiscrete central-upwind schemes for hyperbolic conservation laws and Hamilton–Jacobi equations, *SIAM Journal on Scientific Computing*, 23, 707–740, 2001.
- Maeno, F. and Imamura, F.: Tsunami generation by a rapid entrance of pyroclastic flow into the sea during the 1883 Krakatau eruption, Indonesia, *Journal of Geophysical Research: Solid Earth*, 116, 2011.
- Mandeville, C., Carey, S., Sigurdsson, H., and King, J.: Paleomagnetic evidence for high-temperature emplacement of the 1883 subaqueous
835 pyroclastic flows from Krakatau Volcano, Indonesia, *Journal of Geophysical Research: Solid Earth*, 99, 1994.
- Mangeney, A., Bouchut, F., Thomas, N., Vilotte, J. P., and Bristeau, M. O.: Numerical modeling of self-channeling granular flows and of their levee-channel deposits, *Journal of Geophysical Research*, 112, F02 017–21, <https://doi.org/10.1029/2006JF000469>, 2007.
- Marino, B., Thomas, L., and Linden, P.: The front condition for gravity currents, *Journal of Fluid Mechanics*, 536, 49–78, 2005.
- Michel-Dansac, V., Berthon, C., Clain, S., and Foucher, F.: A well-balanced scheme for the shallow-water equations with topography,
840 *Computers & Mathematics with Applications*, 72, 568–593, 2016.
- Murillo, J. and García-Navarro, P.: Energy balance numerical schemes for shallow water equations with discontinuous topography, *Journal of Computational Physics*, 236, 119–142, 2013.
- Neri, A., Esposti Ongaro, T., Cerminara, M., and de’ Michieli Vitturi, M.: Multiphase flow modeling of explosive volcanic eruptions, in: *Transport phenomena in multiphase systems*, pp. 243–281, Springer, 2022.
- 845 O’Brien, J. S., Julien, P. Y., and Fullerton, W.: Two-dimensional water flood and mudflow simulation, *Journal of hydraulic engineering*, 119, 244–261, 1993.
- Pareschi, L. and Russo, G.: Implicit–explicit Runge–Kutta schemes and applications to hyperbolic systems with relaxation, *Journal of Scientific computing*, 25, 129–155, 2005.
- Patra, A. K., Bauer, A., Nichita, C., Pitman, E. B., Sheridan, M., Bursik, M., Rupp, B., Webber, A., Stinton, A., Namikawa, L., et al.: Parallel
850 adaptive numerical simulation of dry avalanches over natural terrain, *Journal of Volcanology and Geothermal Research*, 139, 1–21, 2005.
- Pitman, E. B., Nichita, C. C., Patra, A., Bauer, A., Sheridan, M., and Bursik, M.: Computing granular avalanches and landslides, *Physics of Fluids*, 15, 3638–9, <https://doi.org/10.1063/1.1614253>, 2003.
- Pudasaini, S. P. and Hutter, K.: *Avalanche dynamics: dynamics of rapid flows of dense granular avalanches*, Springer Science & Business Media, 2007.
- 855 Putra, Y. S., Beaudoin, A., Rousseaux, G., Thomas, L., and Huberson, S.: 2D numerical contributions for the study of non-cohesive sediment transport beneath tidal bores, *Comptes Rendus Mécanique*, 347, 166–180, 2019.
- Shimizu, H., Koyaguchi, T., and Suzuki, Y.: The run-out distance of large-scale pyroclastic density currents: a two-layer depth-averaged model, *Journal of Volcanology and Geothermal Research*, 381, <https://doi.org/10.1016/j.jvolgeores.2019.03.013>, 2019.
- Shimizu, H. A., Koyaguchi, T., and Suzuki, Y. J.: A numerical shallow-water model for gravity currents for a wide range of density differ-
860 ences, *Progress in Earth and Planetary Science*, 4, <https://doi.org/10.1186/s40645-017-0120-2>, 2017a.
- Shimizu, H. A., Koyaguchi, T., and Suzuki, Y. J.: A numerical shallow-water model for gravity currents for a wide range of density differences, *Progress in Earth and Planetary Science*, 4, 1–13, 2017b.
- Sigurdsson, H., Houghton, B., McNutt, S., Rymer, H., and Stix, J.: *The encyclopedia of volcanoes*, Elsevier, 2015.
- Simpkin, T. and Fiske, R.: *Krakatau 1883: The volcanic eruption and its effects*, Smithsonian Institution Press, 1983.
- 865 Sulpizio, R., Dellino, P., Doronzo, D., and Sarocchi, D.: Pyroclastic density currents: state of the art and perspectives, *Journal of Volcanology and Geothermal Research*, 283, 36–65, 2014.
- Toro, E. F.: *Riemann solvers and numerical methods for fluid dynamics: a practical introduction*, Springer Science & Business Media, 2013.



- Valentine, G. A.: Stratified flow in pyroclastic surges, *Bulletin of Volcanology*, 49, 616–630, 1987.
- Von Storch, H. and Woth, K.: Storm surges: perspectives and options, *Sustainability Science*, 3, 33–43, 2008.
- 870 Woods, A. W. and Wohletz, K.: Dimensions and dynamics of co-ignimbrite eruption columns, *Nature*, 350, 225, 1991.
- Woods, A. W., Bursik, M. I., and Kurbatov, A. V.: The interaction of ash flows with ridges, *Bulletin of Volcanology*, 60, 38–51, 1998.
- Zeitlin, V.: *Geophysical fluid dynamics: understanding (almost) everything with rotating shallow water models*, Oxford University Press, 2018.



Table 1. List of model variables with notation and units.

Symbol	Variable	Units
h	flow thickness	m
B	topography elevation	m
t	time	s
u, v	horizontal velocity components	m/s
T	flow temperature	K
T_a	atmospheric air temperature before entrainment	K
T_b	water vapour temperature before entrainment	K
T_i	water temperature	K
P	ambient pressure	Pa
ρ_m	volumetric averaged flow density	kg/s
ρ_a	air density	kg/s
ρ_{wv}	water vapour density	kg/s
ρ_{s,i_s}	i_s solid class density	kg/s
α_a	air volume fraction	
α_{wv}	water vapour volume fraction	
α_{s,i_s}	i_s solid class volume fraction	
C_v	mixture specific heat	$Jkg^{-1}K^{-1}$
C_a	air specific heat	$Jkg^{-1}K^{-1}$
C_{wv}	water vapour specific heat	$Jkg^{-1}K^{-1}$
C_{s,i_s}	i_s solid class specific heat	$Jkg^{-1}K^{-1}$
R_a	air specific gas constant	$Jkg^{-1}K^{-1}$
R_{wv}	water vapour specific gas constant	$Jkg^{-1}K^{-1}$
g	gravitational acceleration	ms^{-2}
g'	reduced gravity	ms^{-2}
E_a	atmospheric air entrainment rate	m/s
E_{wv}	water vapour entrainment rate	m/s
D_{s,i_s}	i_s solid class deposition rate	m/s
F_x, F_y	friction forces per unit area	$kgm^{-1}s^{-2}$
f	friction coefficient	
ϵ	entrainment air coefficient	
Ri	Richardson number	
$\gamma_{i_s,wv}$	i_s solid class vaporization coefficient	
L_w	water specific latent heat of vaporization	Jkg^{-1}
C_D	gas particle drag coefficient	
Re	Reynolds number	
d_s	particle diameter	m
ν	kinematic viscosity coefficient of atmospheric air	m^2s^{-1}